J. Fluid Mech. (2003), *vol.* 484, *pp.* 1–39.
DOI: 10.1017/S0022112003004178 Printed in the United Kingdom

Near-wall physics of a shear-driven three-dimensional turbulent boundary layer with varying crossflow

By ROBERT O. KIESOW[1] AND MICHAEL W. PLESNIAK[2]†

[1]Curtiss-Wright Electro-Mechanical Corporation, Cheswick, PA 15024, USA

[2]School of Mechanical Engineering, Purdue University, West Lafayette, IN 47907, USA.

(Received 7 February 2002 and in revised form 17 December 2002)

The near-wall physics and turbulence structure of a planar shear-driven three-dimensional turbulent boundary layer (3DTBL) with varying strengths of crossflow are examined in a specialized facility. Spanwise shear modifies the near-wall turbulence structure. Flow visualization reveals a reduction of mean streak length by as much as 50%, while streak spanwise spacing remains constant. Power spectra of velocity confirm this shift towards higher temporal frequencies, corresponding to decreased streamwise length scales. Particle image velocimetry (PIV) measurements indicate that the spanwise shear increases the number and strength of flow structures that interact in the inner region of the boundary layer. This leads to increased momentum transfer between low- and high-speed fluids, resulting in a thickening of the inner region of the boundary layer. In addition, the organized two-dimensional boundary layer spanwise vorticity layer along the wall surface is disrupted and forms strong vortical structures that are lifted off the wall surface and diffuse into the boundary layer with streamwise distance. The transverse vorticity experiences a similar alteration. Streamwise velocity profiles exhibit an increasing velocity deficit with increased crossflow, consistent with the thickening of the inner region of the boundary layer. Increases in the normal Reynolds stresses are associated with interaction of the secondary flow structures and modifications to vortical structures with increasing three-dimensionality and higher relative wall speed. Significant increases are observed for the most highly sheared cases with translating wall velocities 2.0 and 2.75 times the free-stream velocity. This increase in the normal stresses leads to an increase in the turbulent kinetic energy over the belt surface, which diffuses into the inner region of the boundary layer with streamwise distance. The Reynolds shear stresses also exhibit a significant increase in magnitude over the belt surface owing to enhanced turbulence production over the translating wall section. In general, three-dimensional effects are confined to the area close to the wall and the crossflow increases the interaction of secondary flow structures leading to modifications of the vorticity in the inner region of the boundary layer. These flow distortions disrupt the near-wall streak structure and result in increased levels of turbulent kinetic energy and Reynolds stresses, particularly over the translating wall section.

1. Introduction and objectives

Complex three-dimensional turbulent boundary layers (3DTBLs) are prevalent in many high-Reynolds-number flows of engineering interest. Examples of such flows

† Author to whom correspondence should be addressed: plesniak@ecn.purdue.edu.

include swept wings, curved ducts, bow and stern regions of ships, wing/body junctions on aircraft and submarine hulls, and endwalls in turbomachinery. Although the mean velocity field and the Reynolds stress tensor have been successfully measured in various boundary-layer flows with three-dimensionality, there remains a dearth of complete turbulence data. Consequently, experimental studies of 3DTBLs continue to be necessary in order to expand the experimental database. In particular, studies that examine the individual effects of pressure gradient, curvature, and crossflow, and how their presence modifies turbulence structure, are warranted. In addition to experimental investigations, various numerical studies have effectively simulated several computationally efficient 3DTBL flows. However, attempts at developing general three-dimensional turbulence models have been largely unsuccessful. Additional complementary experimental and computational efforts are necessary for an effective robust three-dimensional turbulence model to be developed.

The three-dimensionality in 3DTBLs can result from a cross-stream pressure gradient or from spanwise shear, or from a combination of the two. In either case, the low-momentum fluid near the surface is deflected through a greater angle than the faster moving free-stream fluid resulting in a skewed boundary layer. Although three-dimensional turbulent boundary layers are common in engineering flows, the scope of the literature concerning the physics of turbulence is surprisingly small in comparison to that for two-dimensional flows. Johnston & Flack (1996) discuss previous 3DTBL studies and also summarize several unresolved issues. These include the individual effects of pressure gradient and crossflow, and how the presence of crossflow modifies the turbulent 'eddy' structures that lead to the observed reduction of the ratio of turbulent shear stress to turbulent kinetic energy (a_1 structure parameter).

A variety of pressure-driven studies of 3DTBLs have been performed over the past decade or so and can be separated by how the spanwise pressure gradient was generated. Wedge flows were examined by Anderson & Eaton (1987, 1989) and Compton & Eaton (1997). 3TDBLs generated by bends in ducts were investigated by Schwarz & Bradshaw (1993, 1994) and Flack & Johnston (1993, 1994). Flack & Johnston (1993) also studied the flow over a swept step as did Webster, DeGraaff & Eaton (1996), who examined the flow over a swept bump. The three-dimensional flow field over a wing–body junction has been investigated by Ölçmen & Simpson (1992, 1995). The other type of 3DTBL is shear-driven, and early examples include rotating axial cylinder studies by Bissonnette & Mellor (1974) and Lohmann (1976). More recent rotating cylinder studies were performed by Driver & Hebbar (1987, 1989), as well as Driver & Johnston (1990). Another type of shear-driven three-dimensional flow is that over a rotating disk, such as the study by Littell & Eaton (1994).

New developments in computational methods such as direct numerical simulation (DNS) and large-eddy simulation (LES), have led to an increase in numerical studies of 3DTBLs. Examples include computational studies of plane channel flow subject to transverse pressure gradient by Moin *et al.* (1990) and Sendstad & Moin (1992). A similar DNS of plane channel flow subject to both spanwise shear and transverse strain was performed by Coleman, Kim & Le (1996). LES studies of 3DTBLs have been performed by Wu & Squires (1997, 1998) on an equilibrium 3DTBL and a swept bump flow simulating that of Webster *et al.* (1996). Other recent numerical investigations of three-dimensional boundary layers include those by Le (1999) and Le, Coleman & Kim (1999) and Coleman, Kim & Spalart (2000). A recent computational study that shares many geometrical similarities with the present experimental study of the shear-driven 3DTBL is that of Kannepalli & Piomelli (1999, 2000) in which

they performed an LES of a spatially developing, shear-driven turbulent boundary layer.

These aforementioned 3DTBL studies exemplify some of the fundamental characteristics of three-dimensional turbulent boundary layers. Among these is the non-alignment of the strain rate with the shear stress, where the shear stress typically 'lags' the mean-flow strain rate. Another 3DTBL feature is a structure parameter, a_1, defined as the ratio of the magnitude of the shear stress to twice the turbulent kinetic energy ($a_1 = \overline{u'v'}/q^2$) and is essentially a measure of the efficiency of the flow in producing turbulent shear stresses. For a 2DTBL flow, the value of a_1 is typically 0.15. Most three-dimensional flows, however, exhibit a value for the structural parameter that is significantly less than 0.15, indicating that the shear stresses decay faster than in two-dimensional flows. The decrease in a_1 varies from experiment to experiment, and values as low as 0.05 (Anderson & Eaton 1989) have been reported in strongly skewed flows, indicating that skewing has a significant effect on the structure of turbulence. Issues remaining to be resolved include the relative contributions of the individual effects of pressure gradient and crossflow and how they should be incorporated into a turbulence model. In a similar vein, the question remains as to how the crossflow modifies the turbulent 'eddy' structures that lead to the observed reduction of the ratio of turbulent shear stress to turbulent kinetic energy. A better grasp of the physics of the turbulence structure in 3DTBLs, particularly in the near-wall region, is key to developing turbulence models for these complex flows.

A brief review of 2DTBL turbulence structure serves as a foundation for understanding how mean-flow three-dimensionality affects the near-wall turbulence in 3DTBLs. The structure model for two-dimensional flows was reviewed by Robinson (1991). The streamwise velocity field in the viscous sublayer and buffer region of the boundary layer is organized into alternating streaks of low- and high-speed fluid. A significant portion of turbulence production occurs in the buffer region by intermittent events known as ejections and sweeps, or simply the bursting process. An ejection is a rapid outrush of low-momentum fluid, including lifting of low-speed streaks, from the wall to the high-momentum fluid in the outer region. In contrast, a sweep is an inrush of high-momentum outer-layer fluid at a shallow angle towards the wall. These events are associated with horseshoe-shaped vortices whose trailing, quasi-streamwise legs are adjacent to the wall. Thus, the near-wall region, where shear stresses and turbulence production are largest, is dominated by quasi-streamwise vortices. Either sign (clockwise or counterclockwise) of vortex occurs with equal probability.

The turbulent structure in 3DTBLs is essentially a distorted version of the structure in 2DTBLs. In his shear-driven 3DTBL study, Lohmann (1976) suggested that the effect of the transverse shear was to break up the larger quasi-streamwise vortices into smaller structures. Bradshaw & Pontikos (1985) hypothesized that eddies were tilted away from their preferred alignment by the spanwise strain, which impeded shear stress production. Anderson & Eaton (1989) postulated that the mean longitudinal vorticity near the wall in a 3DTBL impedes the formation of streamwise vortices with the opposite sign of rotation, resulting in the observed reduction of the shear stresses. In a continued effort to elucidate turbulent boundary-layer structure issues, Eaton (1995) reviewed several experiments in order to explain how three-dimensionality affects the turbulent boundary-layer structure.

The distortion of turbulence structure by the onset of three-dimensionality was observed by Flack & Johnston (1993) in the flow approaching a 45° swept step. Asymmetry between positive and negative longitudinal vorticity was observed, with vortices having the same sign as the crossflow producing significantly larger ejections.

The DNS by Sendstad & Moin (1992) also exhibited strong asymmetry between vortices of different sign. In addition, reductions in the Reynolds shear stress were shown to be caused by changes in fluid particle trajectories near longitudinal vortices. The rotating disk study by Littell & Eaton (1994) also exhibited asymmetries. They suggested that the stress-producing structures in 3DTBLs favour either a sweep or ejection, depending on the sign of the vorticity of the quasi-streamwise leg of the horseshoe vortex. In a continuation of that study, Chiang & Eaton (1996) showed that the boundary layer in the rotating disk flow has the same general character as that found in 2DTBLs, except for a clear asymmetry in the near-wall structure. The three-dimensionality results in vortices of one sign that are much weaker than those of the other sign, resulting in a reduced efficiency of the boundary layer to produce shear stress.

In summary, attached 3DTBLs contain low- and high-speed streaks and quasi-streamwise vortices that dominate the near-wall region. In addition, the crossflow produces asymmetries in the vortex structures and a reduction in the length scales. Based on these findings, Eaton (1995) concluded that (i) the reduction in the shear stress by mean flow three-dimensionality is not a disequilibrium effect, (ii) the turbulent structure is not distorted unless there is significant skewing in the near-wall region and (iii) the distortion would be reduced with increased Reynolds number. The LES by Wu & Squires (1997) supports the proposed 3DTBL structural model put forth by Littell & Eaton (1994) and Eaton (1995). The LES results confirm a modification of the quasi-streamwise vortices by the three-dimensionality, leaving vortices of one sign producing ejections that contribute more to the turbulent shear stresses, whereas vortices of the other sign are more efficient at producing sweeps. However, most studies have not examined the near-wall region for shear stress reductions.

The present study seeks to clarify the turbulence physics in shear-driven boundary layers in the absence of streamwise pressure gradients. A key issue to be examined is the near-wall behaviour of vortical structures and evaluation of the significance of the interaction between the bottom of the quasi-streamwise vortices at $y^+ \approx 20$ and the tops of the sublayer wall streaks on the turbulence production dynamics. The experimental configuration described here is 'clean', which is conducive to companion computational studies and turbulence modelling efforts, in several respects. First, the effects of skewing (or spanwise straining) are decoupled from the confounding effects of streamwise pressure gradient. Secondly, the planar geometry minimizes the computational complications associated with curvature effects and specification of boundary and initial conditions. Thirdly, the apparatus allows the spanwise strain rate to be varied relative to the streamwise mean shear.

2. Experimental apparatus and techniques

The experiment was performed in a low-speed recirculating water tunnel that provided a flat and smooth test surface along which a well-developed canonical two-dimensional boundary layer was subjected to spanwise wall shear to generate a three-dimensional boundary layer. A detailed facility description is given by Kiesow (1994), in which design considerations and individual tunnel components are discussed. The 467 mm $\times$ 764 mm rectangular test section, made of Super Abrasion Resistant (SAR) acrylic, provided access for optical diagnostics techniques. The Reynolds number based on the momentum thickness at the flow measurement location at the maximum free-stream velocity was $Re_\theta = 1450$ and the boundary-layer thickness was $\delta \approx 50$ mm.

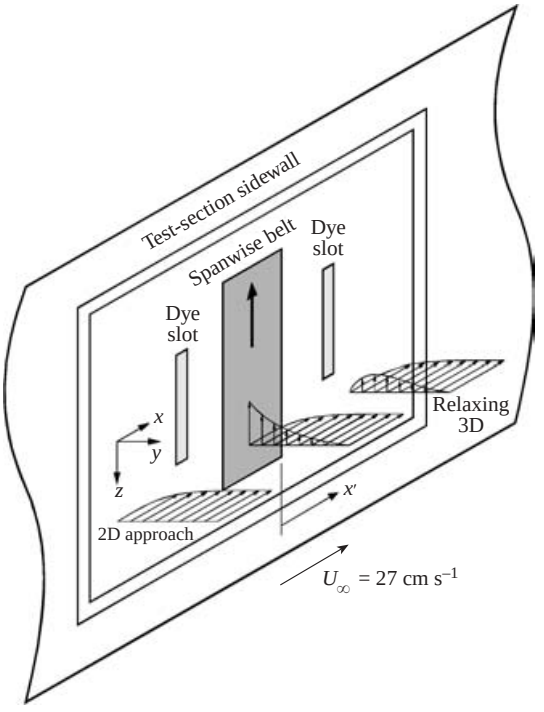

FIGURE 1. Diagram of three-dimensional turbulent boundary-layer test plate.

A 762 mm × 559 mm test plate supported a shearing device integrated into a section of the test section sidewall to provide a spanwise-translating motion, with variable speed capability. A schematic of the shear-driven 3DTBL is shown in figure 1. The shearing device was an enclosed spanwise-translating belt mechanism embedded in the wall with a 127 mm wide by 381 mm high section of the belt exposed in the plane of the test-section sidewall. This corresponds to 50% of the span of the test-section height and approximately two and a half boundary-layer thicknesses in the streamwise direction. A side view diagram of the belt mechanism is shown in figure 2. The shearing device consisted of a drive roller, a tracking idler, and a tensioning idler adjusted by pneumatic cylinders. The tracking assembly provided adjustment capability that ensured that the translating belt ran true in the spanwise direction. A tensioning idler was mounted on a pivoting arm assembly and provided adjustment of the belt tension to ensure that the belt remained flat against the platen. The entire belt assembly was enclosed in its own housing and fully submersed in water during operation so as to avoid air entrainment. The shear-generating mechanism was operated at belt velocity ratios of $W_r = 0$, 1.0, 2.0 and 2.75, where W_r is the spanwise belt speed divided by the free-stream velocity of the boundary layer, $U_\infty = 27\,\mathrm{cm\,s^{-1}}$.

Flow visualization, using direct dye injection and laser induced fluorescence (LIF), was performed to examine the structural features of the shear-driven boundary layer in the near-wall region. Dye was introduced into the flow by means of two 203 mm long dye slots located approximately one-and-a-half boundary-layer thicknesses upstream and downstream of the translating wall, respectively. The dye solution consisted of fluorescein disodium salt dissolved in water at a concentration of 4 p.p.m. A collimated laser light sheet (approximately 1 mm thick and 150 mm wide) oriented in the (x, z)-plane was used to illuminate the fluorescent dye in the near-wall region.

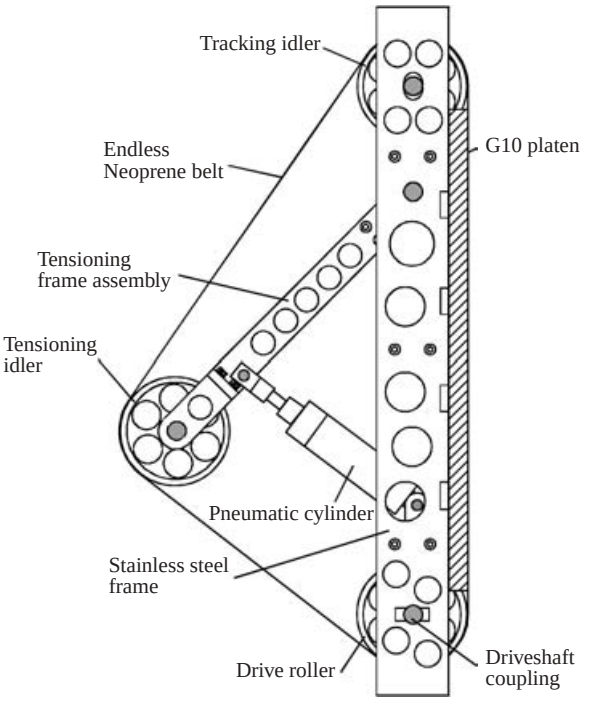

FIGURE 2. Side view of shear-generating mechanism.

Flow visualization images were captured on 8 mm video tape using a Canon® model ES1000 camcorder and on 35 mm ISA 1600 film using a Pentax® ProgramPlus camera with remote shutter release. The high-resolution film images were digitized using an HP Scanjet IIcx.

Hot-film velocity spectra measurements were obtained using a TSI® IFA 300 constant-temperature anemometer. The probe used for this study was a DANTEC 55R01 straight general-purpose single film mounted in a DANTEC probe holder with an extension fitted to allow the hot-film to be positioned on the spanwise centreline of the tunnel. Measurements were obtained at a sampling rate of 20 Hz and low-pass filtered at 10 Hz. A second set of hot-film measurements was acquired at a sampling rate of 200 Hz and low-pass filtered at 100 Hz to provide an expanded frequency range. The resulting frequency resolution was approximately 0.005 Hz for spectra over the 0–10 Hz frequency range and 0.05 Hz for the expanded frequency range of 0–100 Hz.

A particle image velocimetry (PIV) system based on a DANTEC FlowMap PIV 2100 processor was used to obtain instantaneous measurements of two components of velocity in either the (x, y)-plane (parallel and perpendicular to the flow) or the (x, z)-plane (plan view). The optical system consisted of a NewWave 100 mJ Nd:YAG laser system with software-driven controls for the pulse separation time. The laser beam propagated through sheet-forming optics to form a light sheet approximately 1 mm thick and 150 mm wide. A Kodak® MEGAplus ES 1.0 CCD cross-correlation camera, with a 1008(H) $\times$ 1018(V) pixel array provided on-line imaging capability. Controlled image acquisition, storage and display, and processing of the image to obtain the velocity data were accomplished on a personal computer running FlowManager software. The flow was seeded with 5 μm silicon carbide particles at

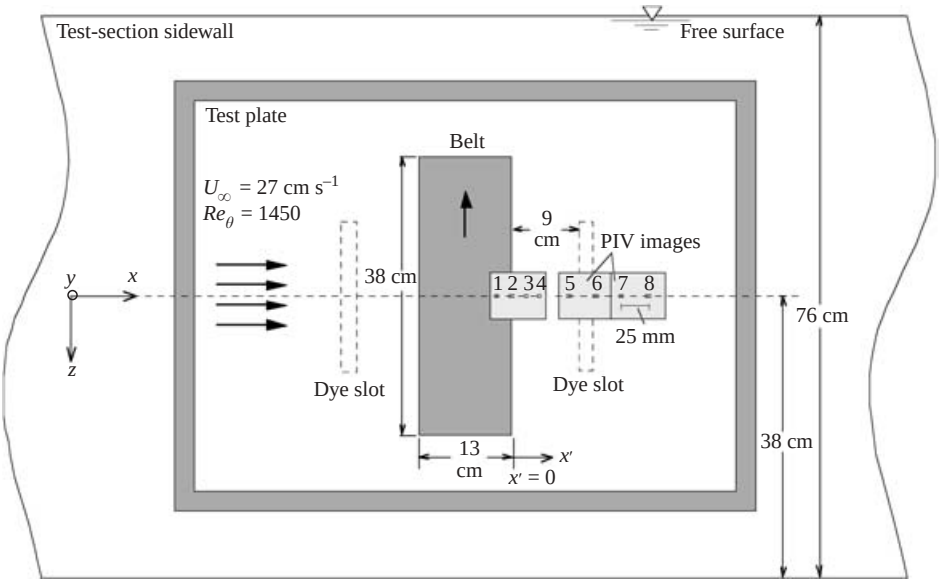

FIGURE 3. Schematic of belt configuration and PIV measurement locations. Measurement stations: 1, $x' = -12.5$ mm; 2, 0 mm; 3, 12.5 mm; 4, 25 mm; 5, 50 mm; 6, 75 mm; 7, 100 mm; 8, 125 mm.

a concentration of approximately 20 particles per mm^3. Vector maps were processed using an interrogation area of 0.84×0.84 mm^2 with 25% overlap, resulting in 6972 vectors in an imaging field of 50×50 mm^2. Typically, 250 images were ensemble-averaged to provide statistics for the mean flow velocity, r.m.s. velocities and Reynolds stresses.

The test geometry and a diagram of the belt configuration are shown in figure 3, including the measurement locations for PIV measurements and corresponding eight streamwise locations where profiles where compiled. In addition, the schematic shows the location of the dye slots used for LIF flow visualization. All measurements are reported in terms of tunnel coordinates where x, y and z are the free-stream, wall-normal and spanwise directions, respectively. The origin for the streamwise coordinate, x', is at the trailing edge of the translating wall. For the y-coordinate, the origin is the test-plate surface and at the spanwise centreline of the test section for the z-coordinate. Although the wall friction velocity is the preferred parameter for normalizing turbulence data, the friction velocity could not be reliably determined in this experimental study. Therefore, the normalization was performed in terms of outer variables using the free-stream velocity, U_∞, and the boundary-layer thickness, δ.

2.1. *Uncertainty*

The uncertainty in the PIV measurements stems primarily from locating the image displacement peak in the cross-correlation field. Velocity vectors in the (x, y)-plane were determined from interrogation spots having a size of 0.84 mm $\times$ 0.84 mm. Displacement errors in Δx and Δy are based on the pixel resolution of the image and are estimated to be no greater than $\pm 2.5\%$. When combined with processing errors, the overall uncertainty in the velocity measurements can be determined at a 95% confidence level following the methods of Moffat (1988). In the (x, y)-plane,

Quantity	$y/\delta = 0.1\,(\%)$	$y/\delta = 0.5\,(\%)$
U	± 5	± 3
V	± 5	± 3
W	± 5	± 3
u'^2	± 12	± 9
v'^2	± 12	± 9
w'^2	± 12	± 9
$-u'v'$	± 30	± 25

TABLE 1. PIV uncertainty estimates.

the uncertainty in the U and V velocities is $\pm 3\%$ of the local measurement. Uncertainties of U and W velocities in the (x, z)-plane are also estimated to be $\pm 3\%$ of the local measurement. Uncertainties in the normal Reynolds stresses u'^2, v'^2 and w'^2 are estimated to be $\pm 9\%$ of the local value. The uncertainty in the primary Reynolds shear stresses, $-\overline{u'v'}$ and $-\overline{u'w'}$, is estimated to be of the order of $\pm 30\%$ of the local measurement. This is a consequence of the limited ensemble size of 250 images to estimate statistical quantities such as second-order moments. These uncertainty estimates are summarized in table 1. The ensemble size chosen represents a compromise between available data storage and processing capabilities and acceptable convergence of statistics. Statistical convergence for PIV data has been addressed, e.g. by Uzol & Camci (2001) and Cater & Soria (2001).

A small number of vectors ($<5\%$) in the (x, y)-plane were discarded owing to unpaired particles and low particle densities in certain interrogation spots. A similar number ($<7\%$) of 'outliers' were present in the (x, y)-plane vector fields, as well. These bad vectors were identified in a post-processing procedure and replaced using an interpolation method. In general, the number of vectors that did not meet prescribed validation criteria increased with increasing spanwise shear. This is attributed to out-of-plane motions arising from increased three-dimensionality.

Measurement uncertainty in the analysis of the LIF flow visualization data arises primarily from determining the streak length. The resolution of measurements of the streamwise length of the streaks in the digitized flow-visualization images is estimated to be ± 1 mm for all streaks and this results in a relative uncertainty of approximately $\pm 5\%$, for a majority of the streaks.

3. Near-wall flow-visualization and velocity spectra

The formation of low-speed streaks in the near-wall region and their interaction with the outer region of the flow through a gradual lift-up and eventual ejection plays an important role in turbulence production and transport of turbulence within the boundary layer of a wall-bounded flow (see Robinson 1991). Laser-induced-fluorescence flow-visualization studies were performed to investigate the effects of crossflow on the near-wall physics of the shear-generated 3DTBL. The dye was introduced into the flow by means of a dye slot located approximately one-and-a-half boundary-layer thicknesses downstream of the translating belt. The flow rate of the dye was adjusted so that the dye fluid seeped through the 0.15 mm (0.005 in) vertical slit of the dye injector into the near-wall region of the turbulent boundary layer so as to minimize velocities perpendicular to the wall. The illuminating laser light sheet was positioned in the (x, z)-plane (parallel to the wall) at y locations of

approximately $y/\delta = 0.01$ and 0.03 from the wall surface. The 150 mm wide light sheet, in conjunction with the 200 mm (spanwise length) dye slot, allowed a significant portion of the near-wall region to be visualized with the fluorescent dye. Belt operating speeds for these studies included a base case with the belt stationary ($W_r = 0$) and velocity ratios $W_r = 1.0$ and 2.0 times the free-stream velocity.

Flow visualization captured on 35 mm film provided the highest resolution images, which were used in subsequent image analysis to quantify the qualitative observations of the flow-visualization work. Representative photographs of the LIF flow visualization for each of the three belt operating conditions and the corresponding digitized image, analysed to reveal the streak contours of the low-speed streaks in the near-wall region, are shown in figure 4. These flow-visualization images are located approximately on the spanwise centreline at the $y/\delta = 0.01$ image plane, and the flow is from left to right. These images show the ubiquitous streaky structure associated with the near-wall region of turbulent flows. Comparison of these images for the three velocity ratios reveals a clear modification of the streak structure due to the crossflow. Streak contours for the $W_r = 0$ case tend to be elongated and maintain their structure for some distance downstream of the dye slot. In comparison, the streak contours for the sheared cases are typically much shorter and are skewed in the direction of the mean flow. The crossflow results in a reduction in the streak length at higher shear rates (a shift towards smaller length scales) compared to the base case of $W_r = 0$. However, there does not appear to be any significant modification of the streak spanwise spacing.

In order to quantify the qualitative observations of the LIF flow visualization, LIF images were digitized and with image enhancement, the wall streaks were identified, counted, and the streak length was measured along the imposed flow direction. Although this procedure entailed a certain amount of subjectivity in identifying a streak and determining its beginning and end, the procedure was applied consistently to all of the images. Therefore, the resulting trends reasonably represent the modifications to the streak structure. Histograms for the streak length for the base case and $W_r = 1.0$ and 2.0 are shown in figure 5. These histograms clearly show a shift towards smaller streamwise length scales with increasing spanwise shear and a narrower distribution of streak sizes compared to the base case. All of the histograms are asymmetric. The $W_r = 2.0$ case exhibits a slightly higher skewness and kurtosis compared to the base case. Statistics of the wall streaks for all three operating conditions are given in table 2 and indicate that the mean streak length $\bar{l}$ is reduced by almost 50% for the strongly sheared case of $W_r = 2.0$. The smaller standard deviations for the sheared cases, along with the reduction in mean streak length, are strong indications of a reduction in the streamwise length scales of the wall streaks in the near-wall region. These statistics confirm the qualitative observations of a modification of the near-wall turbulence structure due to the crossflow as reported in Kiesow & Plesniak (1997, 1998).

The modification of the wall streaks observed in the LIF flow visualization is consistent with the results of the DNS by Sendstad & Moin (1992), as well as by Le *et al.* (1999) of a DNS and LES of a 3DTBL generated by a spanwise-moving wall in a channel flow. The recent LES of a shear-driven 3DTBL by Kannepalli & Piomelli (2000) also includes analysis of near-wall flow structures and wall streaks. They observed significant disruption of near-wall streak structures at the moving/stationary wall junction at both the leading and trailing edge of the moving wall section as the flow adjusts to new wall boundary conditions. The reduction in streak size that is observed in the LES is a trend also observed in the aforementioned LIF flow-visualization

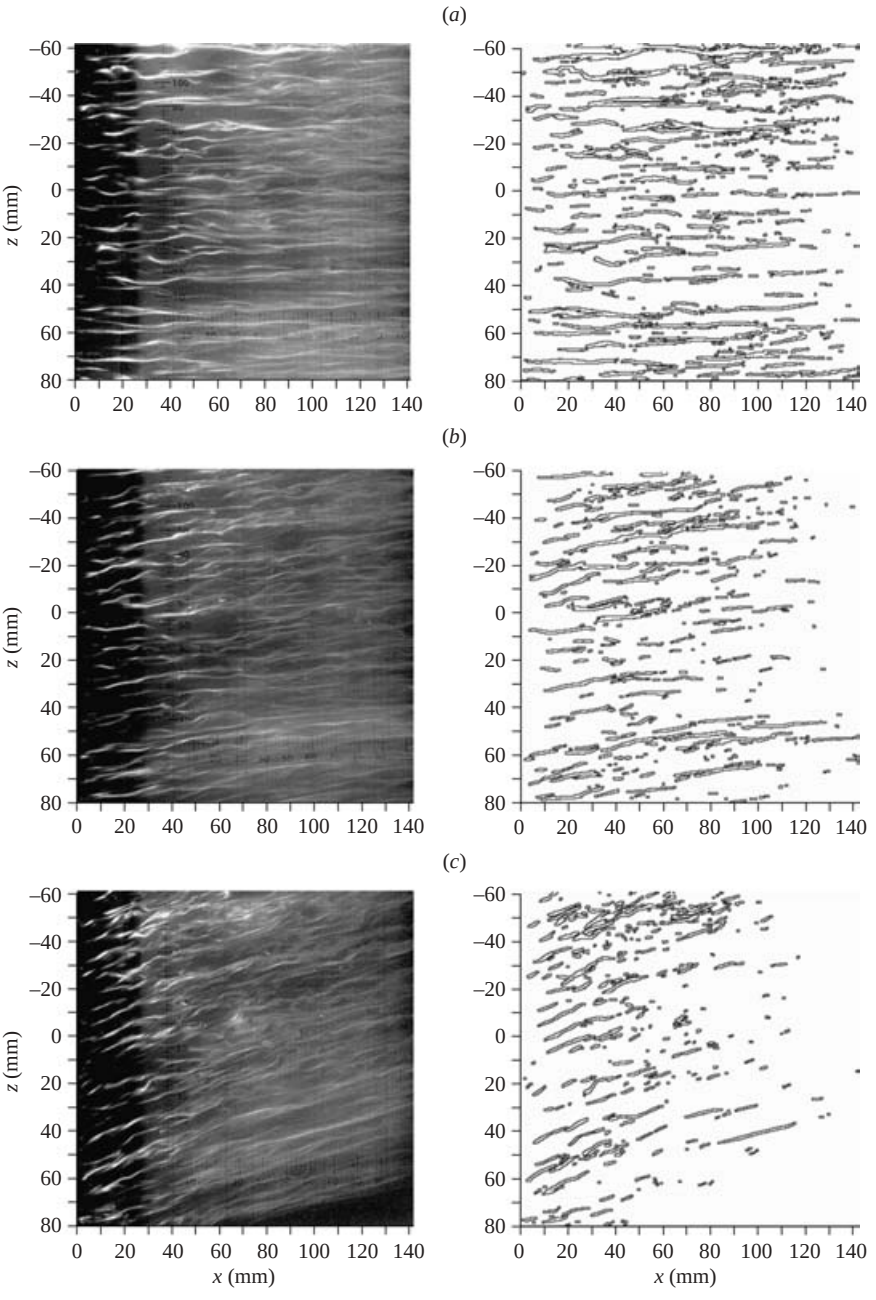

FIGURE 4. LIF photographs and streak contours at $y/\delta = 0.01$ for belt velocities (*a*) $W_r = 0$, (*b*) $W_r = 1.0$ and (*c*) $W_r = 2.0$.

results. Therefore, the current results provide experimental verification of the modification of near-wall structure and a decrease in length scale. However, unlike the LIF flow-visualization results, the LES results of Kannepalli & Piomelli also indicate a significant reduction of streak (spanwise) spacing.

W_r	0	1.0	2.0
$\bar{l}$ (mm)	23.5 ± 1	17.6 ± 1	12.4 ± 1
σ (mm)	14.8 ± 1	10.9 ± 1	7.6 ± 1
Turning angle at $y = 0.5$ mm (deg.)	0	≈ 10	≈ 20

TABLE 2. Low-speed boundary-layer streak statistics for belt operating conditions of $W_r = 0$, 1.0 and 2.0.

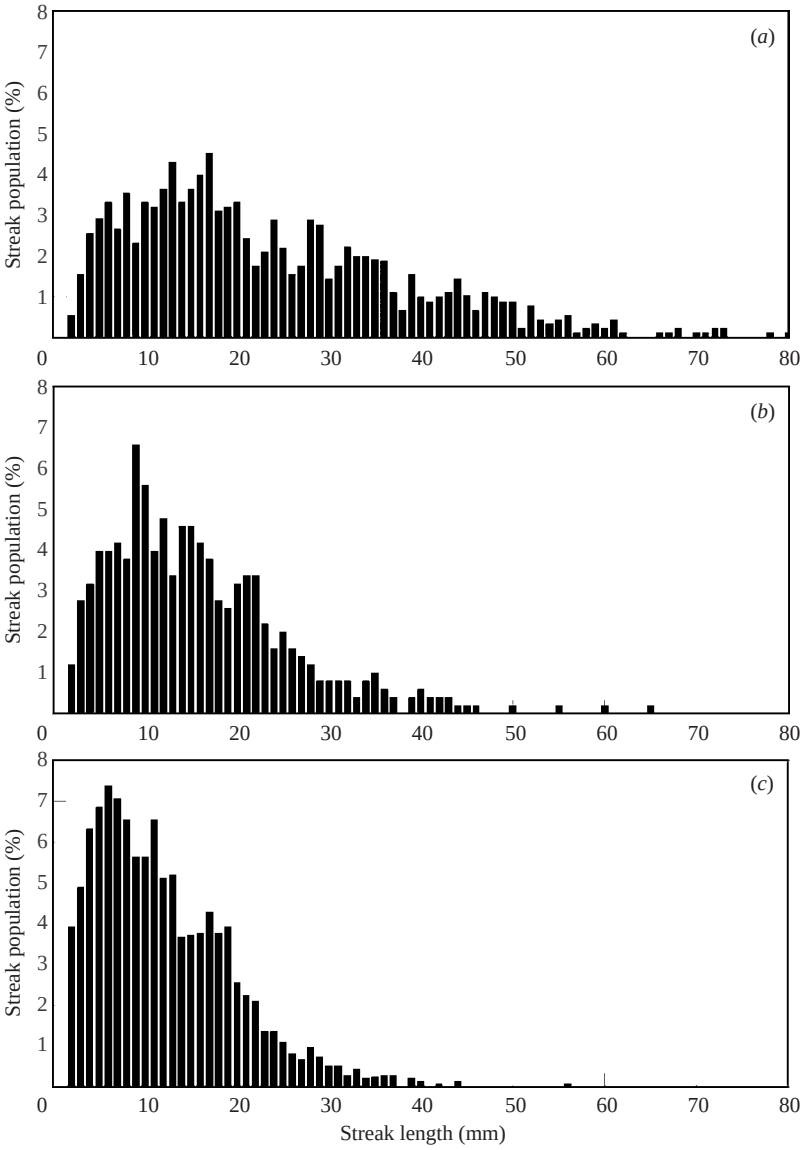

FIGURE 5. Histograms of streak length for belt velocities (*a*) $W_r = 0$, (*b*) $W_r = 1.0$ and (*c*) $W_r = 2.0$.

A more fundamental result of the flow-visualization work is an assessment of the turning angles of the mean flow direction resulting from the application of the spanwise shear. These angles were obtained by measuring the streak orientation in the $y = 0.5$ mm image plane with the positive x-axis as the zero reference. For the $W_r = 1.0$ case, the turning angle is approximately 10°, and increases to approximately 20° for the $W_r = 2.0$ case. These results are also given in table 2.

Hot-film anemometry measurements were used to compute the power spectral density of the streamwise velocity for belt–free-stream velocity ratios of 0.0, 1.0, 2.0 and 2.75. The hot-film probe was located along the spanwise centreline approximately 1.5δ downstream of the trailing edge of the belt, with the centre of the hot-film probe located approximately $y/\delta = 0.12$ ($y^{+0} \approx 80$, superscript 0 refers to normalization using a value based on u_t for the two-dimensional reference case) from the wall surface in the wall-normal direction. The power spectra revealed characteristics of the flow field that are consistent with the aforementioned shift towards smaller streamwise length scales observed in the LIF flow visualization.

Plots of the frequency pre-multiplied one-dimensional power spectra at $y/\delta = 0.12$, over a 0–100 Hz frequency range, are shown in figure 6. The power spectra are non-dimensionalized by the frequency and variance. This normalization locates the peak of the spectrum at the most energetic scales of the flow (corresponding to the -1 slope region in a log–log spectrum). The effect of increasing spanwise shear is to shift the energy peak towards higher frequencies, or smaller streamwise scales. The spectra indicate a shift of the peak energy from about 4 Hz for the two-dimensional case to approximately 10 Hz for the highly sheared cases ($W_r = 2.0$ and 2.75). The frequency spikes that are observed in these spectra are attributed to vibrations of the probe holder owing to vortex shedding (around 30 Hz) and line noise in the TSI® IFA 300 constant-temperature anemometer system (around 60 Hz). Another characteristic observed in the power spectra of the more highly sheared cases is an increase in the energy levels of the flow scales in the boundary layer. With increasing crossflow, the energy in the flow shifts from the lower frequencies (larger scales) to higher frequencies (smaller scales) where the flow becomes more energetic. The effect of imposing increased spanwise shear, based on the velocity spectra, is to cause a progressive growth of the flow energy and to shift the peak energy to higher frequencies. This observation of more energy at the higher frequencies and corresponding smaller scales corroborates the observed shift towards smaller streamwise length scales in the LIF flow visualization and are reported in Kiesow & Plesniak (1999*a*, *b*). Although the physical streak spanwise spacing is expected to be influenced by the crossflow due to an increase in the friction velocity to maintain the value of $z^+ \approx 100$ in a 2DTBL, no significant reduction in spanwise spacing was observed.

4. Velocity field and flow structures

PIV measurements were obtained in order to examine modifications of the near-wall flow structure caused by the three-dimensionality. Two planes of interest were investigated using the PIV system. The first plane, measuring u and v, was parallel to the approach flow and perpendicular to the wall ((x, y)-plane), essentially a cross-section of the boundary layer. These PIV data were used to construct profiles of mean velocities and turbulence statistics at eight streamwise locations along the spanwise centreline as noted in figure 3. The second plane of interest, measuring u and w, was parallel to the approach flow and parallel to the wall ((x, z)-plane) and provided complementary data to the flow-visualization results previously discussed.

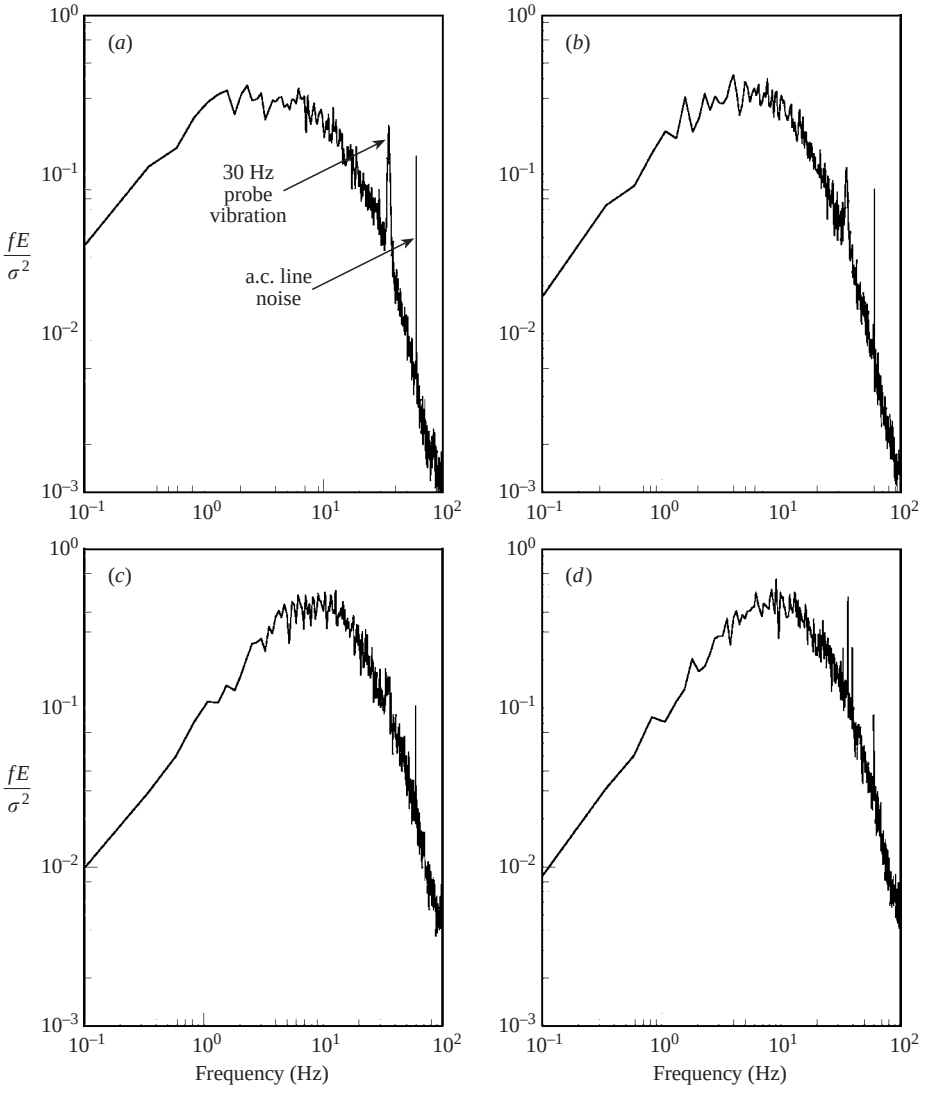

FIGURE 6. Frequency premultiplied power spectra at 1.5δ downstream of belt trailing edge at $y/\delta = 0.12$ from 0 to 100 Hz for velocity ratios (*a*) $W_r = 0$, (*b*) $W_r = 1.0$, (*c*) $W_r = 2.0$ and (*d*) $W_r = 2.75$ from 0.1 to 100 Hz.

These measurements were obtained at the spanwise centreline of the test section, which coincides with the centre of the shearing device, in order to provide a flow region free from end effects where the moving belt interfaces with the test-section sidewall. Measurements were obtained for a base case with the belt stationary ($W_r = 0$) and at belt velocity ratios $W_r = 1.0$, 2.0 and 2.75 times the free-stream velocity, $U_\infty = 27\,\mathrm{cm\,s^{-1}}$.

4.1. (x, y)-*plane measurements*

Representative plots of the fluctuating velocity fields (with the mean subtracted) for the belt stationary case ($W_r = 0$) and belt velocity ratio of $W_r = 2.75$ at $x'/\delta = -0.4$

to 0.6 and $0.8 < x'/\delta < 1.8$ locations are presented in figure 7. In these vector field plots only the inner half of the wall normal image field (corresponding to half the boundary-layer thickness, i.e. $y/\delta < 0.5$) is plotted in order to emphasize the details of the inner region of the boundary layer. The trailing edge of the belt is located at $x' = 0$ ($x'/\delta = 0$) and motion of the belt surface is in the negative z-direction (into the page). The fluctuating velocity field is obtained by subtracting the local velocity mean from each wall-normal location. These data indicate modifications of the inner region of the boundary layer due to the crossflow.

The fluctuating velocity fields for the base case of $W_r = 0$ (figures 7*a* and 7*c*), exhibit fairly regular distributions with small velocity fluctuations spread across the vector field and limited regions of recirculation. The effects of the imposed spanwise shear (crossflow) are most clearly demonstrated in the vector plots of the most highly sheared cases of $W_r = 2.75$, shown in figures 7(*b*) and 7(*d*). The velocity fields exhibit considerably stronger velocity fluctuations throughout the inner region of the boundary layer ($y/\delta < 0.2$) and more numerous and concentrated regions of flow rotation are prevalent and extend into the boundary layer out to $y/\delta \approx 0.3$. Figure 7 indicates a much more active inner region of the boundary layer when crossflow is present, resulting in increased momentum transfer as indicated by structures extending out into the boundary layer and regions of higher-speed fluid moving in towards the wall surface.

The (x, y)-component strain rate is given by $S_{xy} = 1/2(\partial U/\partial y + \partial V/\partial x)$. The gradient of the streamwise velocity in the wall-normal direction, $\partial U/\partial y$, was determined using a second-order centred difference approximation for the inner points and used to represent this strain rate. A first-order forward difference and backward difference approximation was applied to the wall surface points and endpoints, respectively. Contour plots of the resulting velocity gradient are given in figure 8 for velocity ratios of $W_r = 0$ and 2.75 at the $-0.4 < x'/\delta < 0.6$ location. In the two-dimensional case ($W_r = 0$), the primary strain rate is highest, with $\partial U/\partial y$ magnitudes above $50\,\mathrm{s}^{-1}$ in a relatively narrow band along the wall region below $y/\delta \approx 0.05$, which rapidly diminish to near zero levels out into the boundary layer. The two-dimensional cases exhibit a consistently narrow region of strongly positive $\partial U/\partial y$ along the wall region below $y/\delta \approx 0.05$ (typical for a canonical turbulent boundary layer). The strain rate contours in the more highly sheared case of $W_r = 2.75$ are significantly more distorted with numerous isolated regions of both positive and negative sign transported further into the boundary layer to $y/\delta \approx 0.2$. The strain rate plots for the $0.8 < x'/\delta < 1.8$ location (not shown for brevity) continue to exhibit isolated $\partial U/\partial y$ contours which are of reduced magnitude and extend further into the boundary layer with streamwise distance.

Contours of spanwise vorticity, ω_z, are presented in figure 9 for the stationary belt case ($W_r = 0$) and velocity ratio $W_r = 2.75$ at the $x'/\delta = -0.4$ location. Fluctuating velocity vectors are superimposed on top of vorticity contours to show the correlation between secondary flow structures and spanwise vorticity. In the two-dimensional case ($W_r = 0$), strongly negative spanwise vorticity is concentrated in a layer directly along the wall surface. Increased spanwise shear causes the spanwise vorticity to be distributed into more numerous and concentrated regions of both negative and positive vorticity that are lifted away from the wall surface into the inner region of the boundary layer. For the most strongly sheared case of $W_r = 2.75$, the wall layer of spanwise vorticity present in the two-dimensional flow case is completely distorted and disrupted. There are numerous regions of strong negative and positive vorticity, almost like counter-rotating pairs, that extend well into the inner region of the boundary

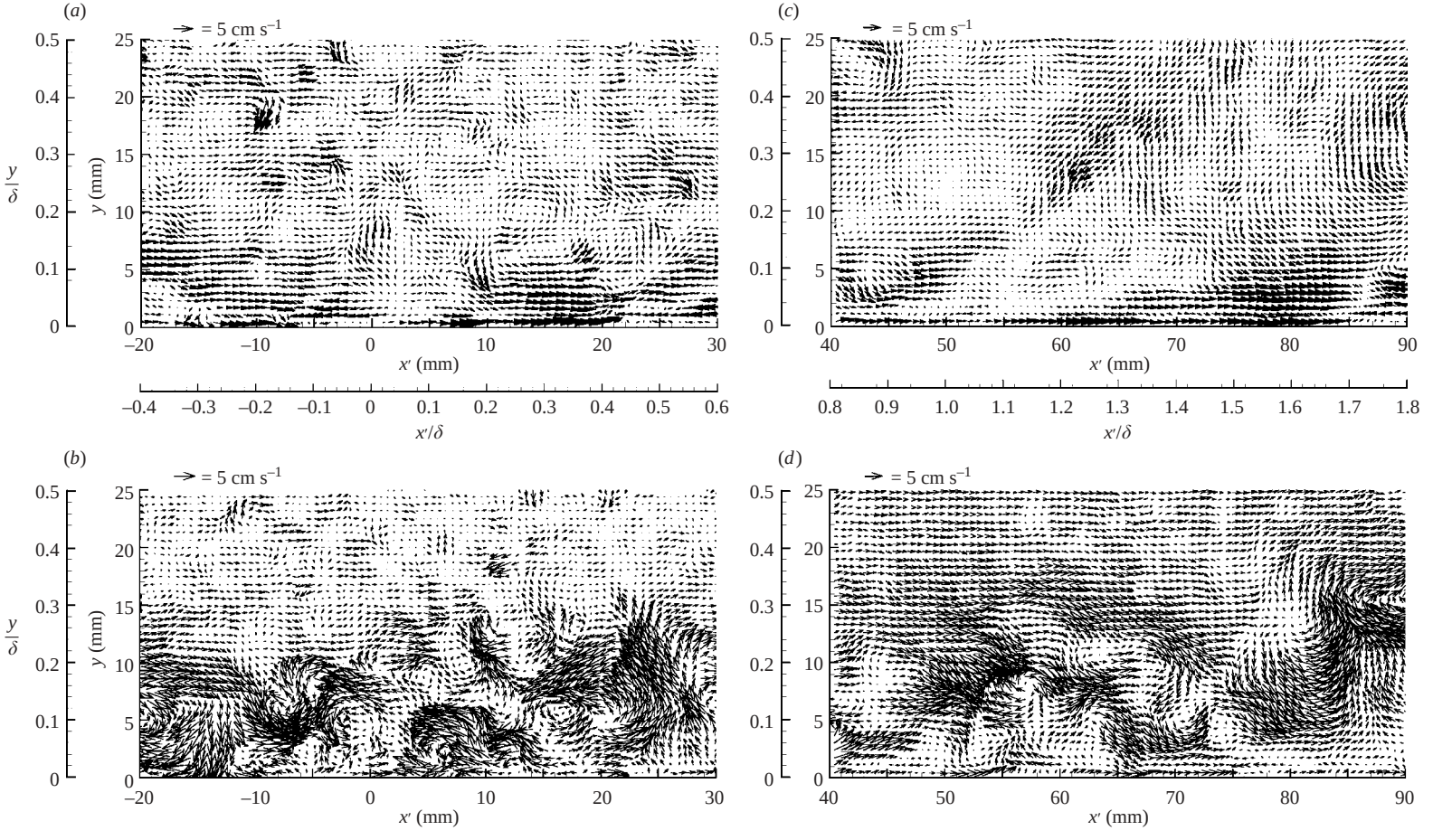

FIGURE 7. Vector maps of fluctuating velocity field in the (x, y)-plane at $x'/\delta = -0.4$ to 0.6 for belt velocity ratios (a) $W_r = 0$ and (b) $W_r = 2.75$ and at $x'/\delta = 0.8$ to 1.8 for belt velocity ratios (c) $W_r = 0$ and (d) $W_r = 2.75$.

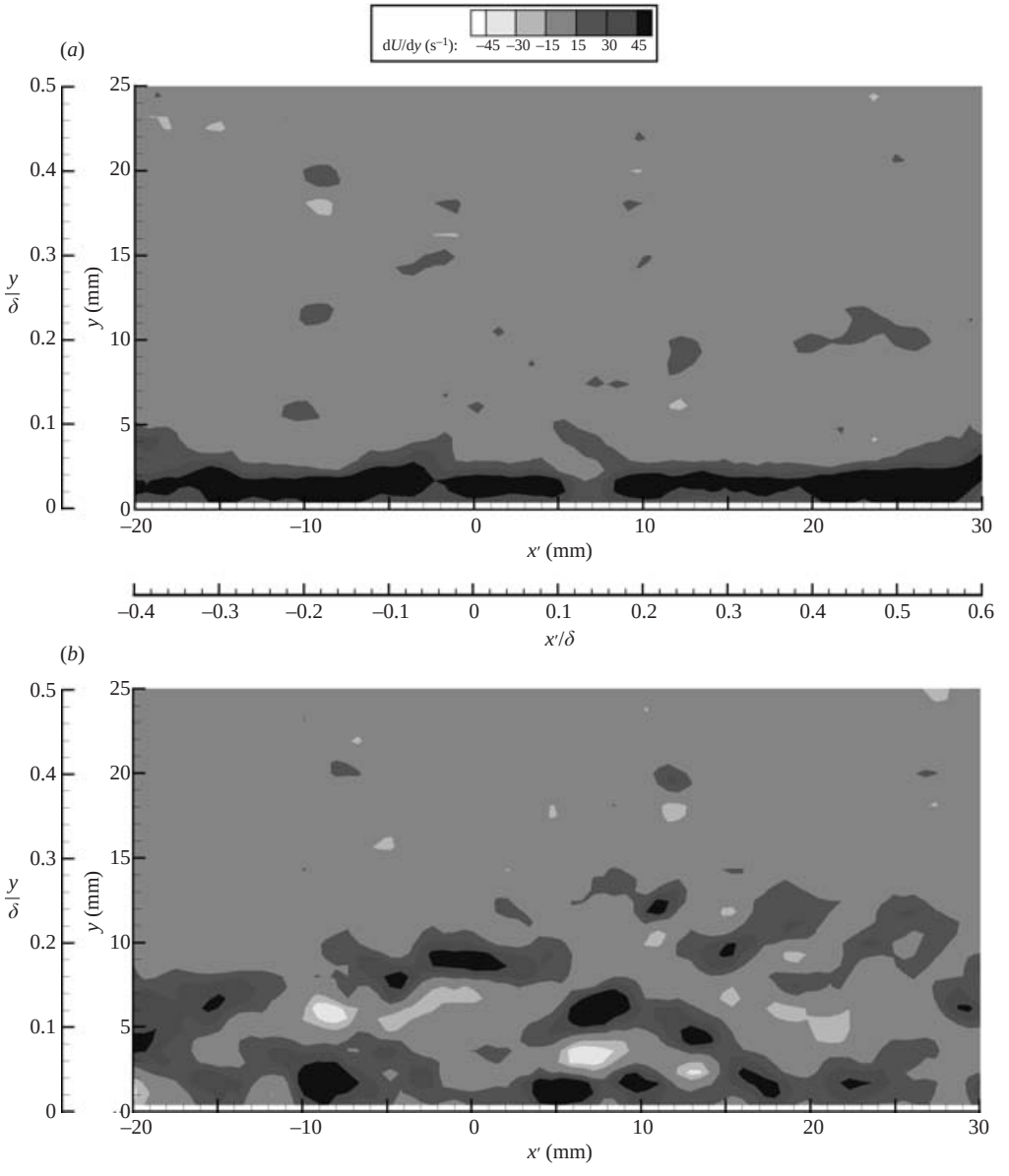

FIGURE 8. Contours of velocity gradient, $\partial U/\partial y$, at $x'/\delta = -0.4$ to 0.6 in the (x, y)-plane for (a) a stationary belt ($W_r = 0$) and (b) belt velocity ratio $W_r = 2.75$.

layer out to $y/\delta \approx 0.2$. The regions of positive and negative vorticity correspond well with structures marked by secondary velocity fields rotating in opposite directions. Contour plots of spanwise vorticity at the $x'/\delta = 0.8$ measurement location indicate similar characteristics to those over the belt surface. The counter-rotating structures observed in both the fluctuating velocity fields and the spanwise vorticity contours are consistent with studies by Adrian, Meinhart & Tomkins (2000) and Zhou *et al.* (1999) in which PIV was used to reveal the formation of hairpin vortices in turbulent boundary-layer flows.

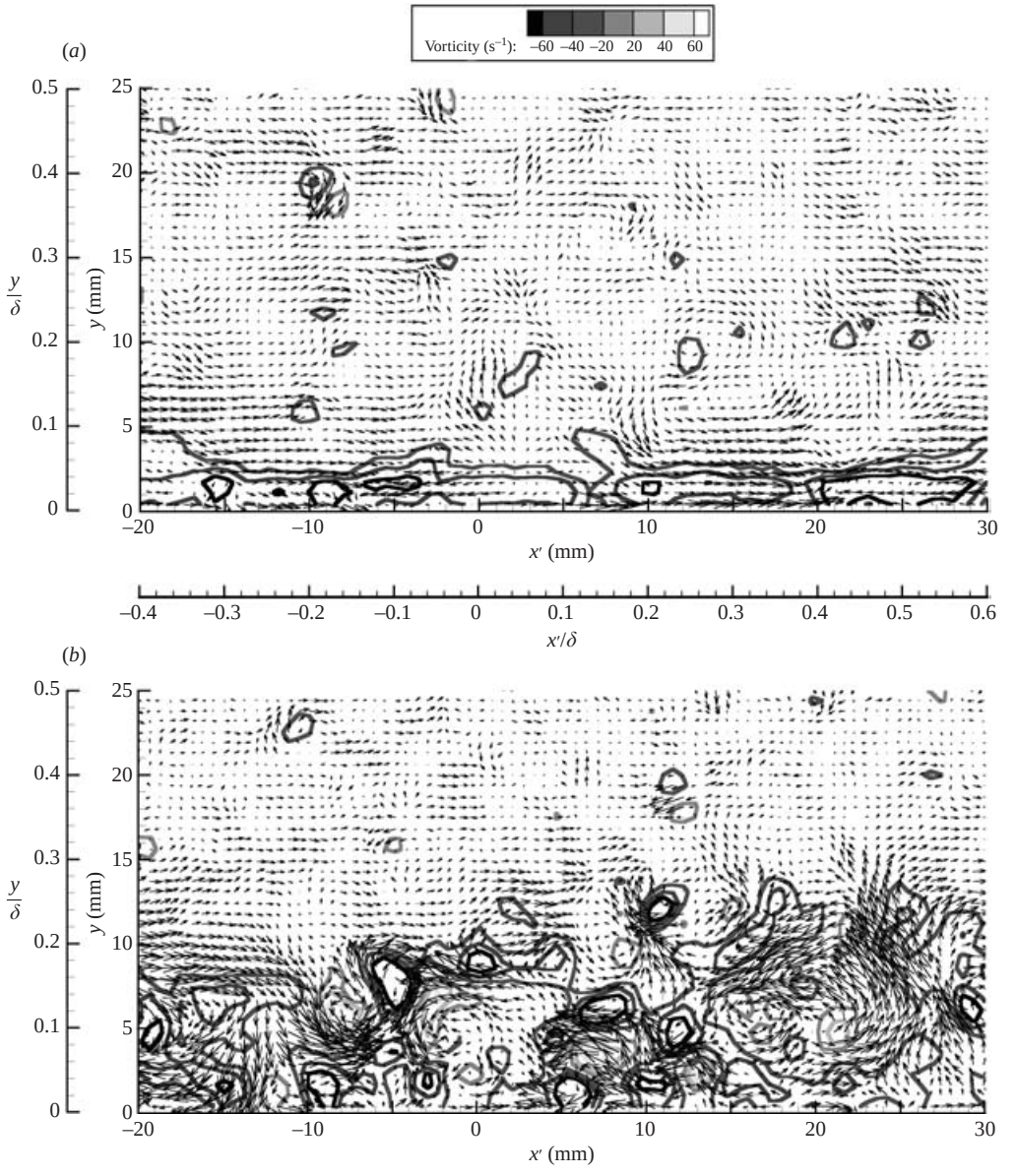

FIGURE 9. Contours of instantaneous spanwise vorticity, ω_z, at $x'/\delta = -0.4$ to 0.6 in (x, y)-plane with superimposed fluctuating velocity vectors for (a) stationary belt ($W_r = 0$) and (b) belt velocity ratio $W_r = 2.75$.

It is hypothesized that the crossflow, which results in the secondary flow structures observed in the (x, y)-plane PIV measurements, induces a strong skewing of the tail section of hairpin structures embedded in the near-wall flow. The effects of the crossflow appear to be confined to a relatively narrow region in the inner region of the boundary layer and are particularly strong over the belt region and just downstream of the moving/stationary wall junction at the trailing edge of the belt. Crossflow, particularly in the higher spanwise shear cases, results in a significant skewing and stretching of the tail region of the hairpin vortices in the direction of the

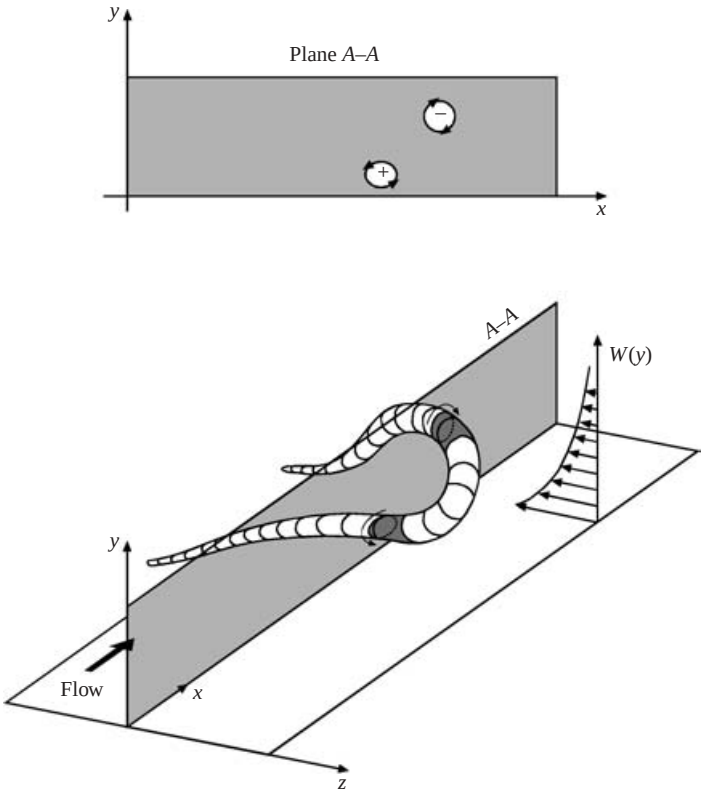

FIGURE 10. Schematic of skewed hairpin vortex in a shear-driven 3DTBL.

spanwise velocity, as indicated in figure 10. The arch region of the hairpin structure remains fairly unaffected considering that the hairpin arch typically extends out to $y^{+0} \approx 250$ (superscript 0 refers to normalization using value based on u_τ for the two-dimensional reference case) and the effects of the crossflow appear to be limited to the boundary-layer region below this. The (x, y)-plane PIV measurements are referenced to fixed tunnel coordinates and not aligned with the mean flow direction. As a result, the (x, y)-plane serves as a cutting plane through the turbulent boundary layer and reveals the cross-sections of the hairpin vortices as regions of the hairpin structure (i.e. the tail, neck and arch) pass through the (x, y)-plane. This cutting plane is shown schematically as section A–A in figure 10. The proposed structural modification results in the observed regions of strong negative and positive spanwise vorticity and associated secondary velocity structures presented in the aforementioned (x, y)-plane measurements and are thus considered to be representative of cross-sections of skewed hairpin vortices in the 3DTBL.

The skewing of these hairpin vortices is also associated with the observed modification of the near-wall streak structure, as discussed previously. The skewing of the tail sections of the hairpin vortices results in a misalignment of the quasi-streamwise vortices, which in the two-dimensional case form extended regions associated with elongated streak structures. The distortion or misalignment of the tail section of the hairpin vortices is reflected in the observed decrease in streamwise length scales.

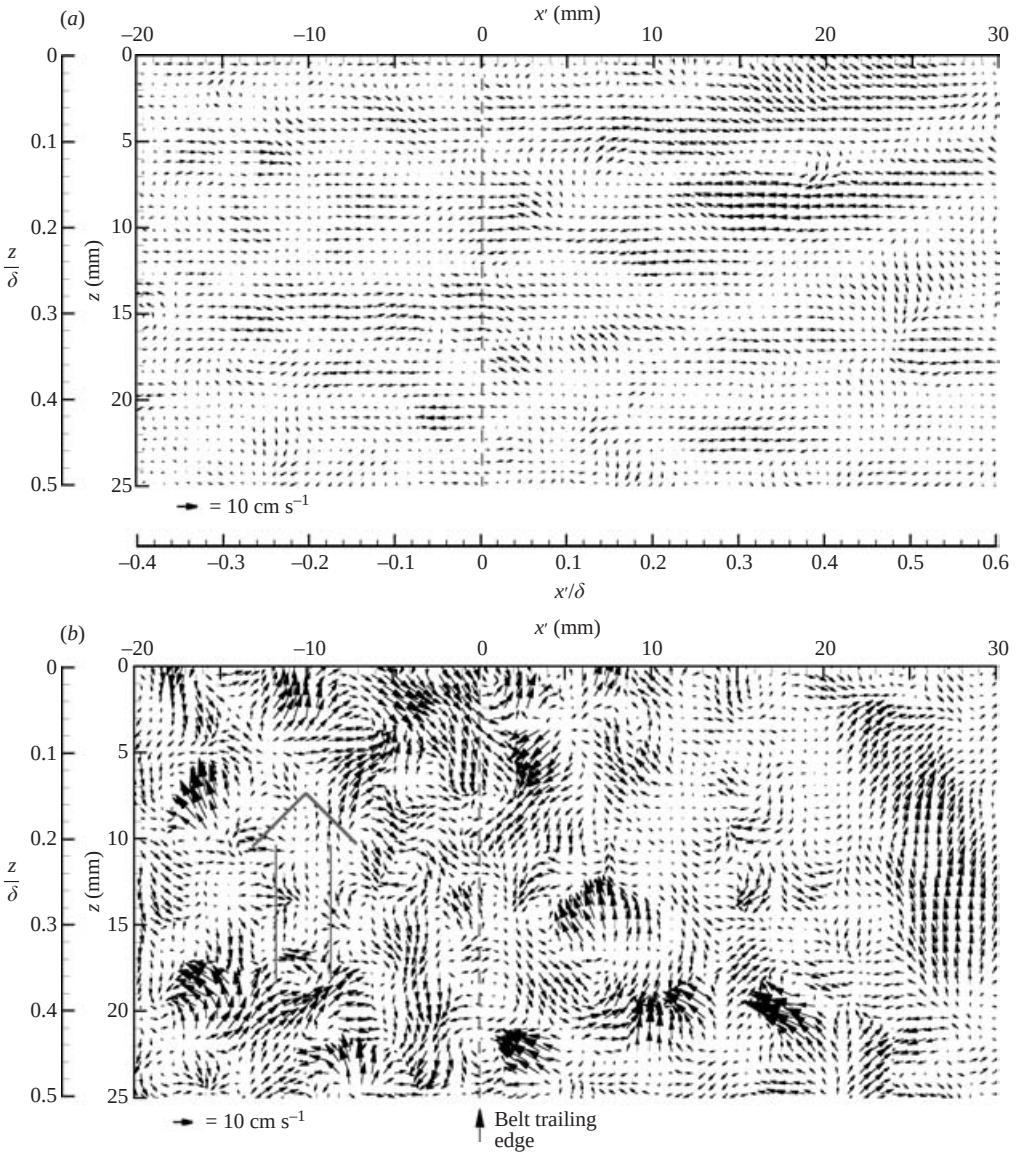

FIGURE 11. Vector maps of fluctuating velocity field at $x'/\delta = -0.4$ to 0.6 in the (x, z)-plane at $y/\delta = 0.01$ for (*a*) a stationary belt ($W_r = 0$) and (*b*) belt velocity ratio $W_r = 2.75$.

4.2. (x, y)-*plane measurements*

PIV measurements were also performed in a plane parallel to the wall ((x, z)-plane) to obtain simultaneous measurements of the u and w components of velocity. Representative plots of the fluctuating velocity fields for velocity ratios of $W_r = 0$ and 2.75 at $x'/\delta = -0.4$ to 0.6 and $y/\delta \approx 0.01$ are presented in figure 11. For brevity, only the lower half of the total spanwise extent of the image region is plotted. The trailing edge of the belt at $x' = 0\,(x'/\delta = 0)$ is indicated by the dashed line and the motion of the belt is in the negative z-direction. The fluctuating velocity field for the two-dimensional base case (figure 11*a*), exhibits mostly small-magnitude fluctuations

with several regions of reduced velocity, which are most probably associated with the near-wall streaky structure of the turbulent boundary layer. The most strongly sheared case ($W_r = 2.75$) in figure 11(b) exhibits the strongest effects of the crossflow. This figure shows numerous concentrated regions of large secondary velocity fluctuations throughout the flow field that are mostly concentrated in the region over the belt surface and do not appear to have any preferential alignment with the mean flow direction.

The spanwise gradient of the spanwise velocity in the z-direction, $\partial W/\partial z$, was determined in the same manner as used to determine the strain rate, represented by $\partial U/\partial y$. This quantity is significant because $\partial W/\partial z$ appears in the production term $\overline{v'w'}\partial W/\partial z$ in the transport equation for the Reynolds stress $\overline{v'w'}$, as well as in the transport equation for $\overline{u'w'}$. Contour plots of the $\partial W/\partial z$ strain rate are plotted in figure 12 for the two-dimensional base case and $W_r = 2.75$ at the $x'/\delta = -0.4$ location at $y/\delta \approx 0.01$. The two-dimensional base case ($W_r = 0$ in figure 12a) exhibits a fairly uniform strain rate field that is nearly zero. The most highly sheared cases of $W_r = 2.75$ in figure 12(b) exhibits strong gradients, particularly over the belt region at $x'/\delta < 0$, in the form of numerous regions of strongly negative and positive $\partial W/\partial z$. Also noteworthy is that the contours of $\partial W/\partial z$ in the $W_r = 2.75$ case do not exhibit any distinct preferential alignment with the mean flow direction.

4.3. *Ensemble-averaged velocity field statistics*

The PIV data discussed in the previous section were further analysed to provide statistical information on the 3DTBL turbulence. Ensemble-averaged measurements in both the (x, y)- and the (x, z)-planes for the three cases with $W_r = 1.0$, 2.0 and 2.75 are compared to the two-dimensional base case ($W_r = 0$). The statistical information included contours of mean velocity magnitude, velocity fluctuations, primary and secondary Reynolds stresses, and two-dimensional turbulent kinetic energy, as well as mean spanwise and transverse vorticity. Although a large sample size is desirable to reduce scatter in the ensemble-averaged data, practical limitations of the data-acquisition system allowed a sample size of only 250 images to be acquired. However, despite these limitations, the sample size is sufficient to garner meaningful data and allow for reasonable interpretation of the results following conclusions from studies by Uzol & Camci (2001) and Cater & Soria (2001) on the effect of sample size on PIV measurements. These authors specifically investigated the effect of ensemble size on PIV statistics for turbulent flow, and conclude that for most cases results based on 250 realizations agree closely with those for 1000 realizations. In addition to contours, profiles of mean velocity, normal Reynolds stresses and Reynolds shear stresses, turbulent shear stress production, anisotropy and mixing length were generated at eight streamwise locations that spanned the three PIV measurement locations (leading edges of the PIV images were at $x'/\delta = -0.4$, $x'/\delta = 0.8$ and $x'/\delta = 1.8$ with respect to the belt trailing edge).

Contours of velocity magnitude for belt velocity ratios of $W_r = 0$, 1.0, 2.0 and 2.75 at all three streamwise locations in the (x, y)-plane are presented in summary form in figure 13. Mild spanwise shear causes a slight expansion of the low-velocity contours (velocities below $0.225\,\mathrm{m\,s^{-1}}$) in the inner region of the boundary layer, indicating a slight thickening of the inner region of the boundary layer. With greater streamwise distance, the low-velocity regions expand slightly further into the boundary layer (out to $y/\delta \approx 0.2$). Increased spanwise shear, $W_r = 2.0$, results in further spreading of low-velocity magnitude contours into the boundary layer, and the contours become more irregular. The most strongly sheared case of $W_r = 2.75$ exhibits the most significant

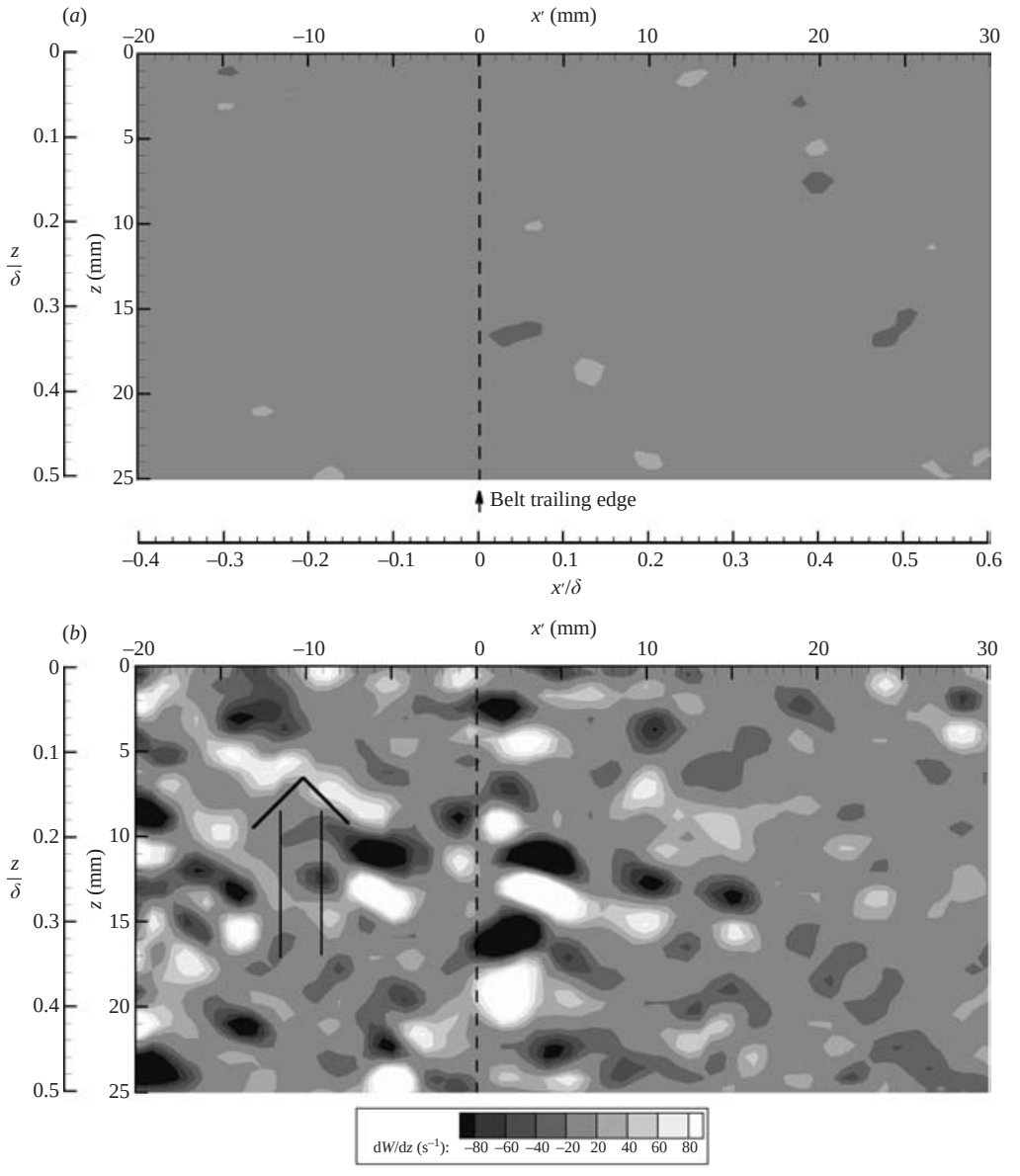

FIGURE 12. Contour plots of $\partial W/\partial z$ at $x'/\delta = -0.4$ to 0.6 in the (x, z)-plane at $y/\delta = 0.01$ for (a) stationary belt ($W_r = 0$) and (b) belt velocity ratio $W_r = 2.75$.

effects of the crossflow. The crossflow results in a significant broadening of the low-velocity contours in the inner region of the boundary layer, indicating a noticeable deceleration of the flow in this region. These effects of crossflow are projected further out into the boundary layer with streamwise distance and the 'low' velocity contours extend out to $y/\delta \approx 0.3$.

Contours of the $(\overline{u'}^2+\overline{v'}^2)/2$, referred to as (two-component) TKE, for the stationary belt case ($W_r = 0$) and the three sheared cases are presented in figure 14. It should be noted that the belt motion introduces significant mean kinetic energy into the flow. The mildly sheared case of $W_r = 1.0$ exhibits a slight increase in TKE levels

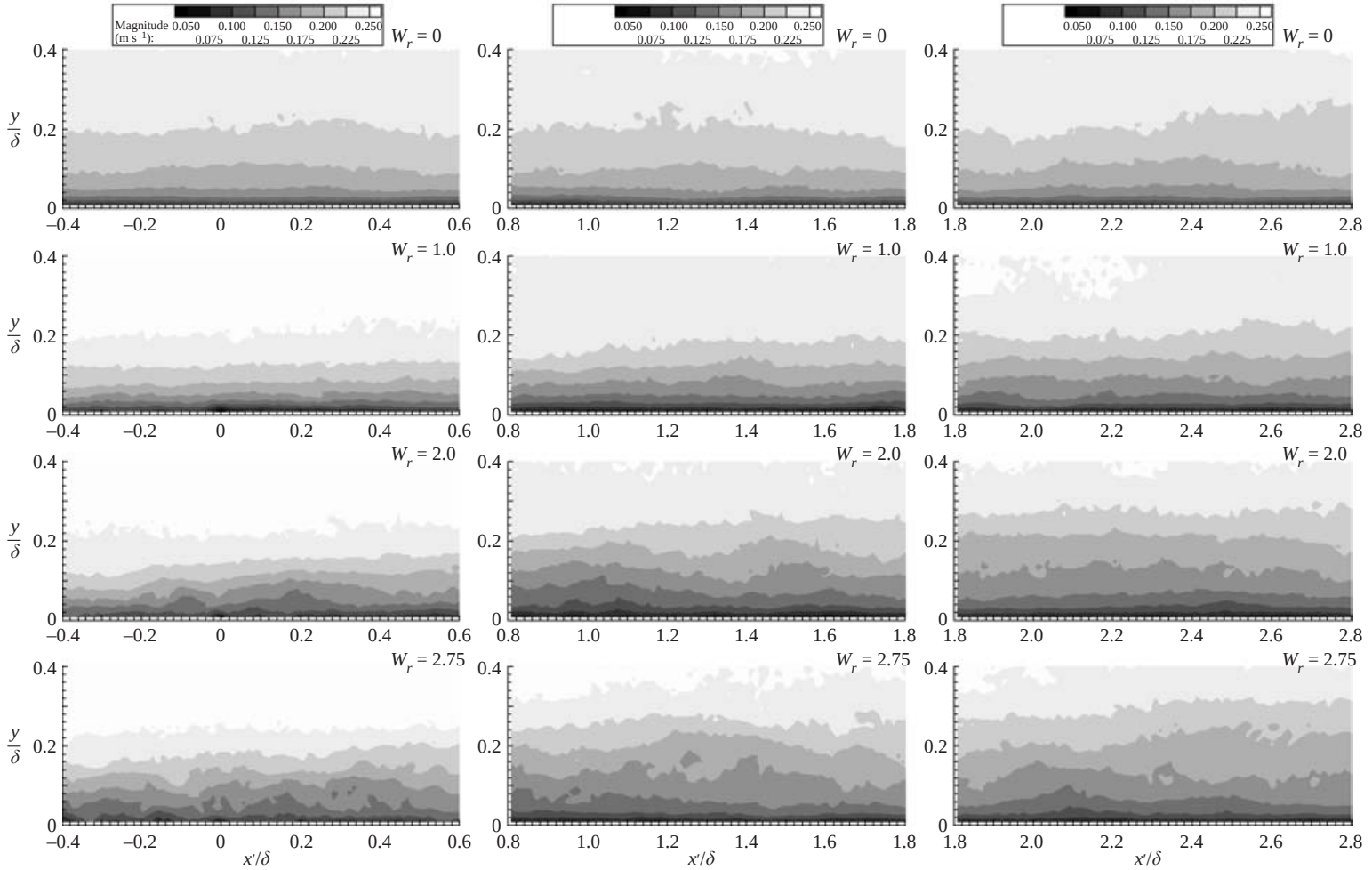

FIGURE 13. Contours of velocity magnitude at streamwise locations $x'/\delta = -0.4$, 0.8, and 1.8 for belt velocity ratios $W_r = 0$, 1.0, 2.0 and 2.75.

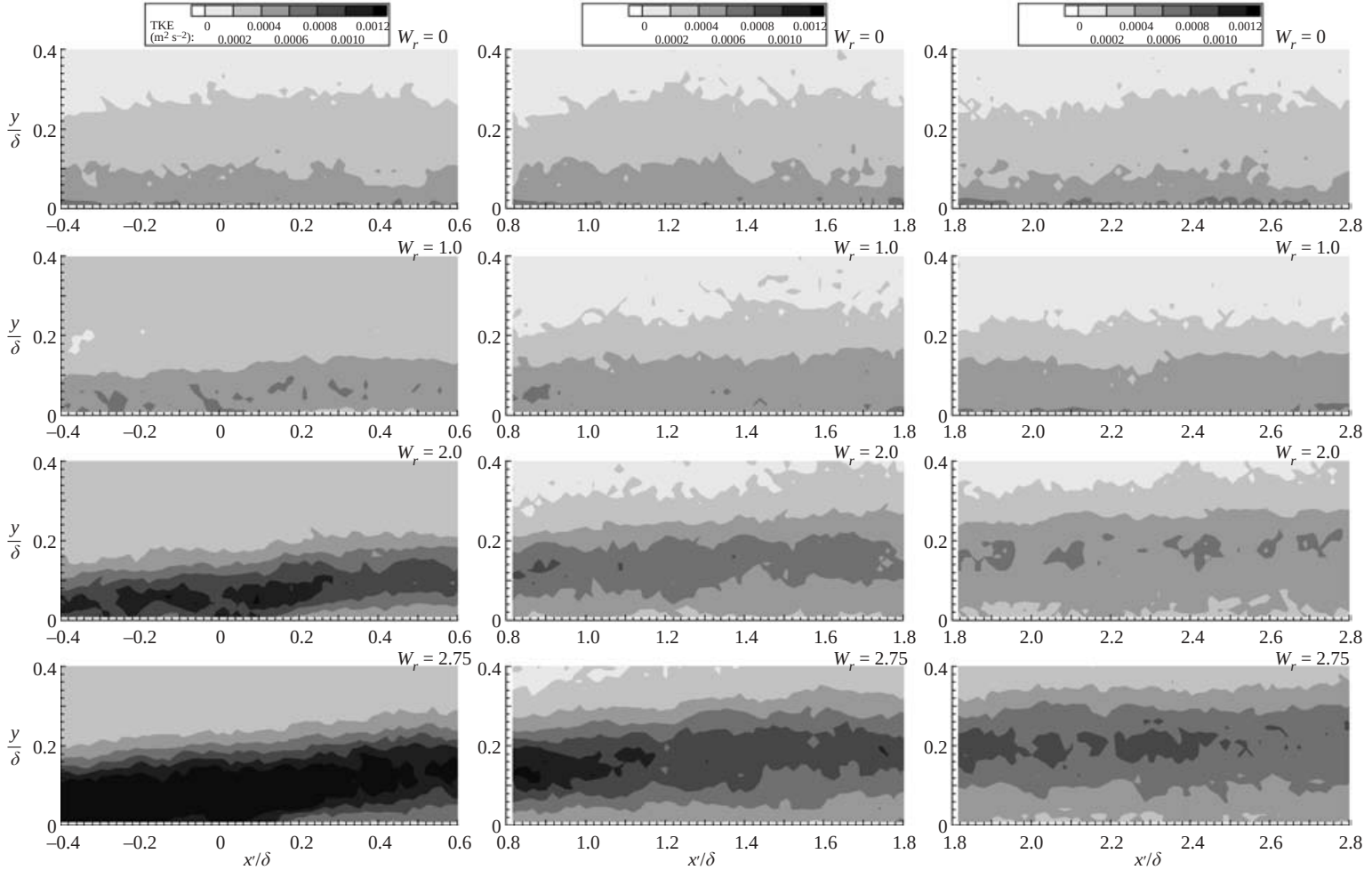

FIGURE 14. Contours of TKE, $(u'^2 + v'^2)/2$, at streamwise locations $x'/\delta = -0.4$, 0.8, and 1.8 for belt velocity ratios $W_r = 0$, 1.0, 2.0 and 2.75.

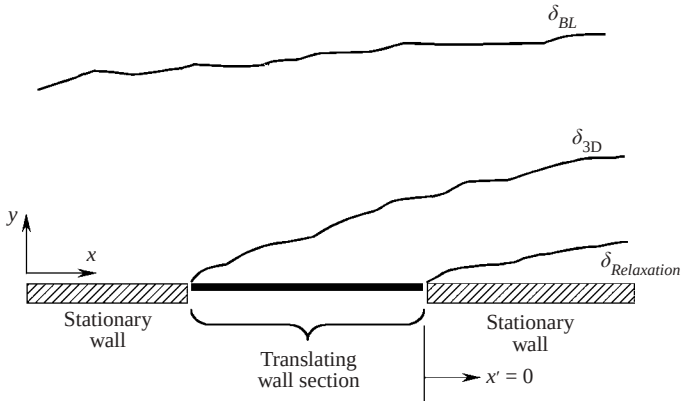

FIGURE 15. Schematic of boundary-layer development near spanwise moving wall.

compared to the $W_r = 0$ case at the $x'/\delta = -0.4$ location. At the two subsequent streamwise locations, the levels of TKE are approximately equivalent to those in the two-dimensional base case. The more highly sheared cases of $W_r = 2.0$ and 2.75 exhibit significantly higher levels of TKE than the two-dimensional base case. For $W_r = 2.0$, peak levels of TKE are of the order of $0.0010\,\mathrm{m^2\,s^{-2}}$ and concentrated over the belt surface below $y/\delta \approx 0.1$. The most highly sheared case of $W_r = 2.75$ exhibits the highest level of TKE, with magnitudes of the order of $0.0012\,\mathrm{m^2\,s^{-2}}$ over the belt region, below $y/\delta < 0.15$. At the belt trailing edge, the TKE levels decrease rapidly to levels upstream of the belt in the near-wall regions as the flow adjusts to the stationary wall condition. With increasing downstream distance, the magnitude of the near-wall TKE begins to decrease as it is convected downstream and into the outer region of the boundary layer. Concentrated regions of increased magnitude are shifted out to $y/\delta \approx 0.2$ for the $W_r = 2.75$ case. These contours of TKE for the most highly sheared cases illustrate the development of a three-dimensional boundary layer within the larger two-dimensional boundary layer of the core flow. At the trailing edge of the moving wall, the boundary layer re-establishes itself along the stationary wall as the three-dimensional effects convect away from the surface. A diagram of the boundary-layer development in the moving wall region is shown in figure 15. In essence, an internal boundary layer that contains the effects of the crossflow is formed within the overall boundary layer and grows with streamwise distance. Consequently, modifications of the flow field because of the presence of crossflow are confined to a relatively narrow region near the wall.

The (x, z)-plane results are presented next. Contours of the u' velocity fluctuations for the cases of $W_r = 1.0$, 2.0 and 2.75 at a y/δ location of 0.01 in the (x, z)-plane are presented in figure 16 for the $x'/\delta = -0.4$ location. The moving belt causes an increase in the streamwise velocity fluctuations in all wall-normal image planes, particularly at the higher imposed shear rates. Of particular note is the significant increase in the streamwise velocity fluctuations over the belt surface and just downstream (a region extending from $x'/\delta = -0.4$ to 0.1) for the $W_r = 2.75$ case at $y/\delta = 0.01$, in which u' fluctuations exceed $5\,\mathrm{cm\,s^{-1}}$. The u' velocities are elevated only slightly with respect to the two-dimensional baseline case in the downstream region ($x'/\delta > 0.2$ and beyond) and decrease with x'/δ distance. The u' fluctuations decrease away from the wall and the contours are distributed in smaller concentrated regions over the belt surface. Downstream of the belt trailing edge at $x'/\delta = 0.8$, the u' velocity fluctuations are

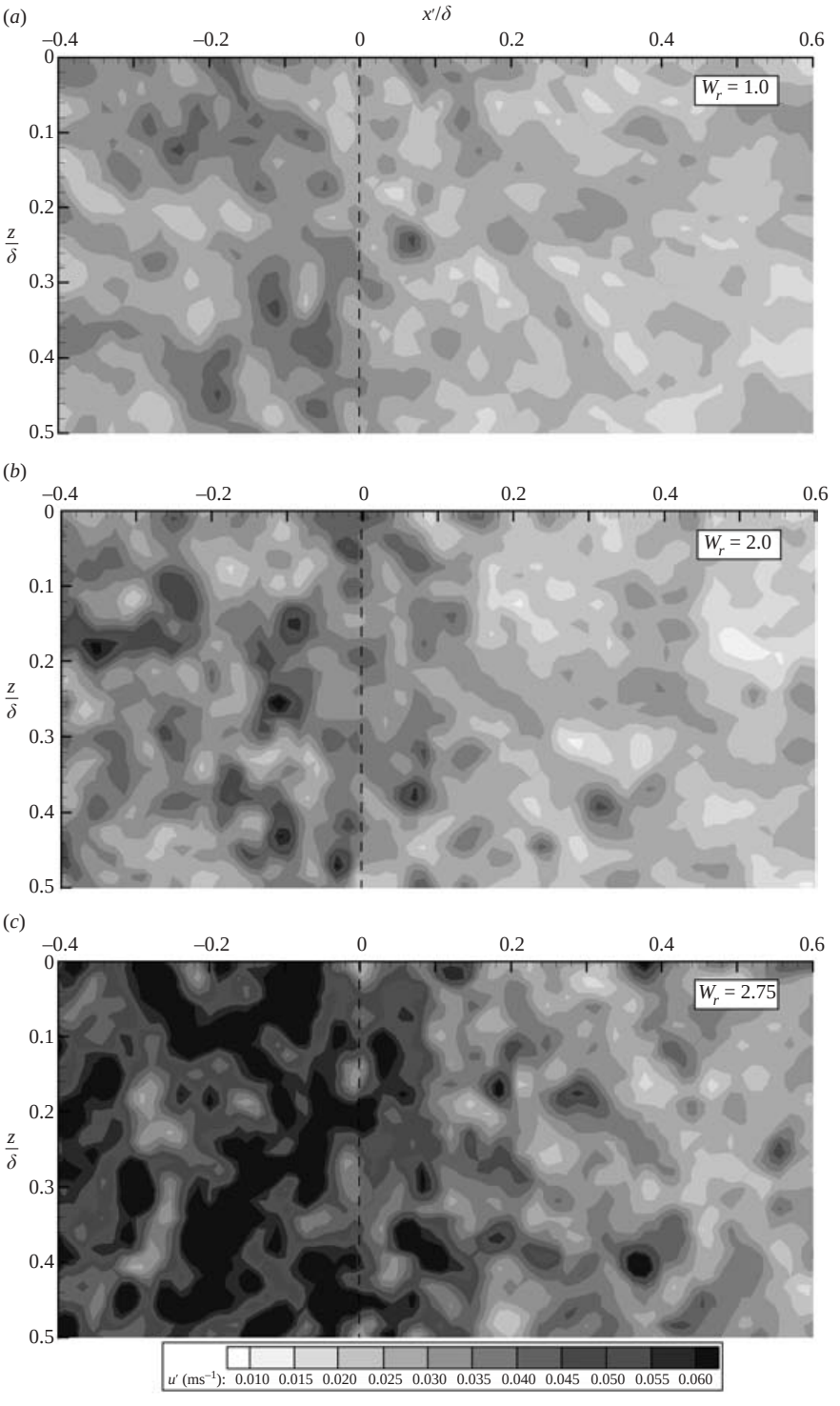

FIGURE 16. Contours of u' fluctuating velocity in $y/\delta \approx 0.01$ image plane at $x'/\delta = -0.4$ to 0.6 for belt velocity ratios (*a*) $W_r = 1.0$, (*b*) $W_r = 2.0$ and (*c*) $W_r = 2.75$.

considerably reduced compared to the upstream values, with magnitudes of the order of only $2\,\mathrm{cm\,s^{-1}}$. Even in the most highly sheared case of $W_r = 2.75$, the increase in the u' fluctuations is minimal, although contours appear to be aligned with the mean flow angle of approximately 45°.

Similar contour plots for the w' velocity fluctuations are shown in figure 17 at the $x'/\delta = -0.4$ location. As for the u' fluctuations at $y/\delta = 0.01$, there is a significant increase in w' with increasing spanwise shear, particularly over the belt region. The mildly sheared case of $W_r = 1.0$ exhibits significant levels of w' (in excess of $5\,\mathrm{cm\,s^{-1}}$) in several adjacent, partially attached contour regions that appear to be aligned 90° to the mean flow angle. With increased spanwise shear, these contours coalesce into large regions of uniformly elevated w' fluctuations. In the case of $W_r = 2.75$, the relatively higher levels of w' fluctuations extend significantly downstream of the trailing edge of the belt. The w' velocity fluctuations at $x'/\delta = 0.8$ and $y/\delta = 0.01$ (not shown) are significantly lower than those over the belt junction. However, w' levels are elevated compared to the two-dimensional base case, with w' magnitudes reaching $2.5\,\mathrm{cm\,s^{-1}}$ for the most highly sheared case of $W_r = 2.75$.

Similar to the spanwise vorticity, the effect of the crossflow is also reflected in the mean transverse vorticity, $\Omega_y = \partial W/\partial x - \partial U/\partial z$, with distinct differences at the different velocity ratios (not shown for brevity). Elongated vorticity contours of both strong negative and positive vorticity become significantly distorted and occur in smaller, more concentrated regions that are randomly distributed across the image field, particularly over the belt region. The transverse vorticity typically does not exhibit a preferential alignment of any kind with increasing spanwise shear. The vorticity levels are significantly reduced with streamwise distance and approach near zero values of the two-dimensional base case of $W_r = 0$. It should also be noted that contours of Reynolds shear stress quantities, such as $-\overline{u'v'}$ and $-\overline{u'w'}$, were also examined, but are not included for brevity. However, these data are associated with larger uncertainties. They are discussed in Kiesow (2000) and Kiesow & Plesniak (2001, 2002).

Boundary-layer profiles of the streamwise velocity for four belt operating conditions of $W_r = 0$, 1.0, 2.0 and 2.75 are shown in figure 18. For conciseness, only four of the eight profile locations are presented here for mean velocity and turbulence parameters. The first three profile locations were compiled from PIV measurements in the first image region. The locations include profiles at $x'/\delta = -0.25$, 0 and 0.25, which cover the region just upstream and downstream of the trailing edge of the translating wall section. The remaining profile location at $x'/\delta = 1.0$ is included to show the development of the relaxing 3DTBL and was compiled from PIV data in the downstream image region with leading edge at $x'/\delta = 0.8$. These profiles of ensemble-averaged velocities and higher-order statistics are plotted along with the benchmark 2DTBL data from the DNS by Spalart (1989). The mean velocity is plotted in dimensionless outer variables using a free-stream velocity $U_\infty = 27\,\mathrm{cm\,s^{-1}}$ and a boundary-layer thickness of $\delta = 50\,\mathrm{mm}$. The boundary-layer thickness over the relatively short measurement distance was not observed to change significantly with streamwise distance or with the strength of the crossflow. Indeed, the overall boundary-layer thickness was essentially unaffected by the presence of the translating wall motion. However, a significant thickening of the inner region of the boundary layer was observed, particularly with higher spanwise shear. This is indicated by profiles of the mean streamwise velocity that develop an increasingly severe velocity deficit in the inner region of the boundary layer with increasing spanwise shear. The velocity deficit for the three sheared cases of $W_r = 1.0$, 2.0 and 2.75 is greatest

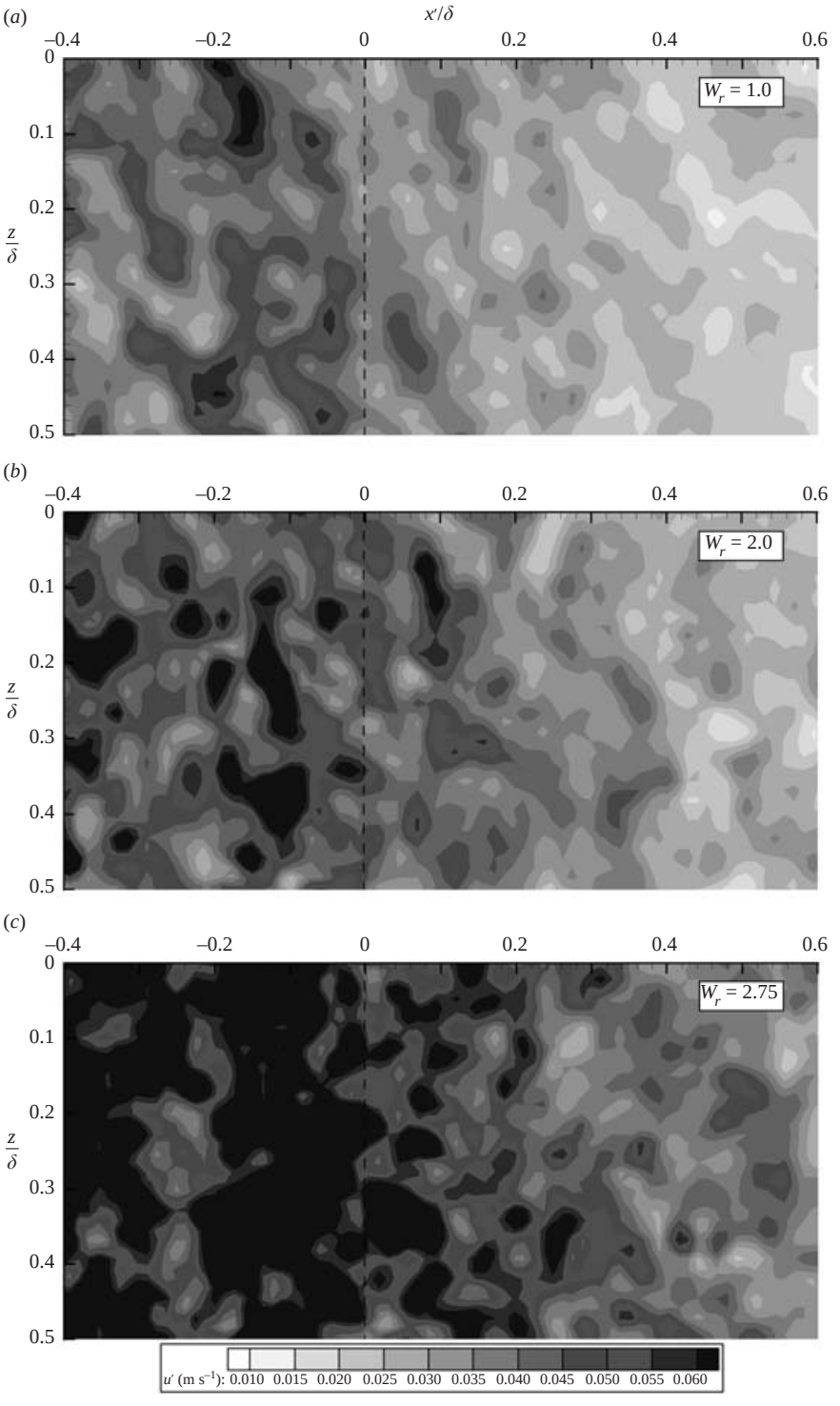

FIGURE 17. Contours of w' fluctuating velocity in $y/\delta \approx 0.01$ image plane at $x'/\delta = -0.4$ to 0.6 for belt velocity ratios (*a*) $W_r = 1.0$, (*b*) $W_r = 2.0$ and (*c*) $W_r = 2.75$.

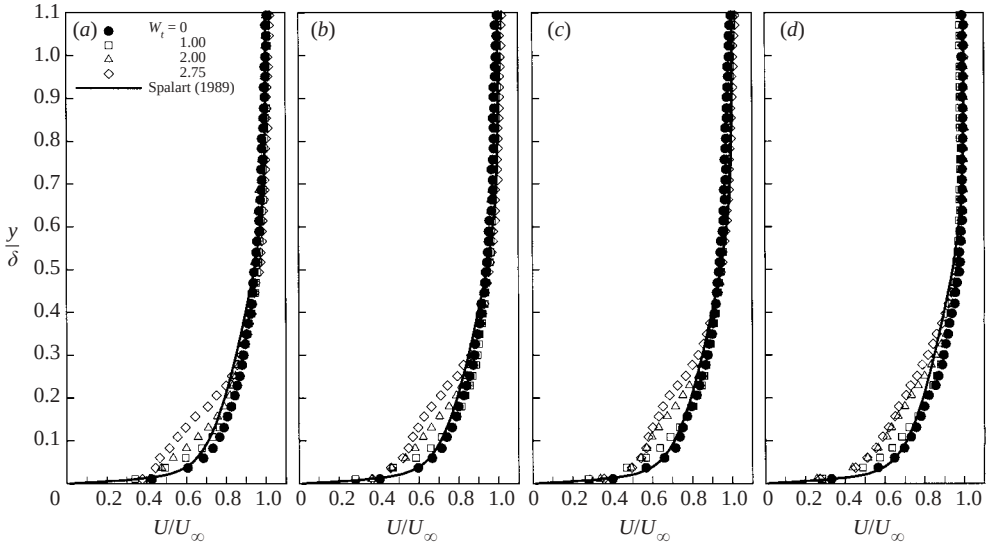

FIGURE 18. Boundary-layer profiles of streamwise velocity at (*a*) $x'/\delta = -0.25$, (*b*) $x'/\delta = 0$, (*c*) $x'/\delta = 0.25$, and (*d*) $x'/\delta = 1.0$ for velocity ratios of $W_r = 0$, 1.0, 2.0 and 2.75.

at the first profile location directly over the belt surface, where the spanwise shear is applied. For the most highly sheared case of $W_r = 2.75$ the velocity deficit is approximately 30% at $y/\delta \approx 0.1$ and extends out to $y/\delta \approx 0.3$. In the outer region of the boundary layer ($y/\delta > 0.4$), the profiles are similar and essentially collapse onto a common curve, indicating that streamwise boundary layer for the sheared cases grows at the same rate as the two-dimensional base case ($W_r = 0$). Shortly downstream of the belt trailing edge (stations 3 and 4) the velocity deficit for the sheared cases is still pronounced and the effects of the crossflow have convected further into the boundary layer ($y/\delta \approx 0.4$). However, in the near-wall region of the boundary layer, the streamwise velocity begins to recover from the spanwise shear and returns to a fuller turbulent boundary-layer profile. A strong velocity deficit is still evident at the higher imposed shear cases at the remaining streamwise locations of one boundary-layer thickness and beyond (i.e. $x'/\delta = 1.0$). However, the magnitude of the deficit of the streamwise velocity begins to decrease, indicating a relaxation of the three-dimensional flow.

These streamwise velocity profiles share many features of a two-dimensional boundary-layer subject to adverse pressure gradient, as evidenced by the rapid thickening of the inner region of the boundary layer and the retarded flow near the wall. Lohmann (1976) and Anderson & Eaton (1987) have observed similar boundary-layer development in a 3DTBL. The observed streamwise boundary-layer development is perhaps best explained by consideration of a momentum balance. In the absence of a streamwise pressure gradient, the only explanation is that the velocity deficit in the streamwise velocity profile results from an increase in the streamwise wall shear stress. The increased wall shear stress is a consequence of increased turbulence production in the wall region, which was measured in this shear-driven 3DTBL. Increased turbulence production and an associated increase in the streamwise drag are features reported for a fully developed shear layer in the LES of a 3DTBL by Le (1999) which was subjected to spanwise shear by a moving wall. The streamwise

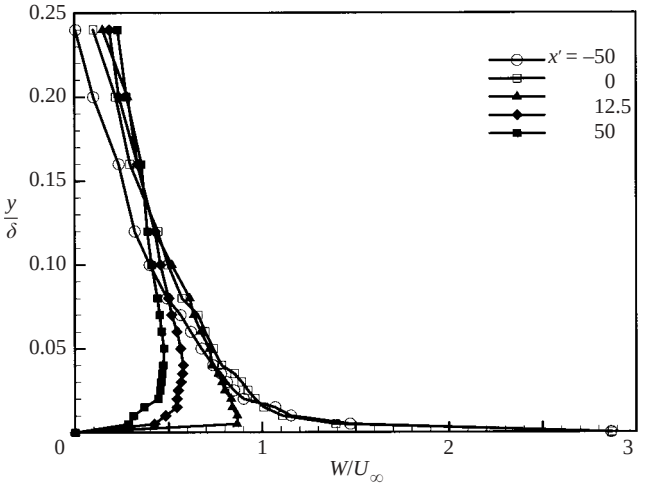

FIGURE 19. Profiles of spanwise velocity for velocity ratio of $W_r = 2.75$.

velocity profiles of the LES exhibited a velocity deficit as observed in the current investigation.

Boundary-layer profiles of the spanwise velocity in the inner region of the boundary layer (out to $y/\delta \approx 0.25$ for velocity ratio $W_r = 2.75$) are plotted in figure 19 in terms of outer variables at several streamwise measuring stations. The spanwise velocity is highest at the first two measuring stations of $x'/\delta = -0.5$ and 0 with a belt velocity ratio for the most highly sheared case $W_r \approx 2.75$. Just downstream of the belt trailing edge, the spanwise velocity magnitude near the wall is nearly the same as the free-stream velocity of $U_\infty = 27\ \mathrm{cm\,s^{-1}}$ and decreases rapidly with streamwise distance. For all the streamwise measurement locations, the spanwise velocity magnitude rapidly decreases, i.e. $W/U_\infty \leqslant 0.30$ at $y/\delta \approx 0.2$ and beyond. The decrease of spanwise velocity by a factor of five by a y-normal distance of $y/\delta \approx 0.05$ emphasizes that the effects of the spanwise shear are confined to a very thin layer along the wall surface. This is further exemplified by the magnitude of the spanwise mean strain rate in this region, which is approximately of the order of $\partial W/\partial y \approx -9.5\,\mathrm{s^{-1}}$ for $y/\delta < 0.01$ and rapidly decreases to $\partial W/\partial y \approx -0.5\,\mathrm{s^{-1}}$ for $y/\delta > 0.03$. Downstream of the belt trailing edge ($x' = 50$ and 75 mm), the spanwise velocity component has decreased to approximately 0.4 U_∞. However, the decay of the spanwise velocity component is not as severe as for the upstream measuring stations as the effects of the skewing diffuse out into the boundary layer, although the decrease is appreciable.

The mean velocity profiles for the most highly sheared case ($W_r = 2.75$) are also presented in the form of a hodograph, figure 20, which shows the spanwise component of velocity as a function of the streamwise component. This polar plot clearly indicates the non-equilibrium state of the flow over and near the translating belt section. The nonlinear shape of the hodograph profiles at $x'/\delta = 0$ and 0.25 indicates the non-collateral condition resulting from the strong three-dimensionality in the near-wall region of the boundary-layer characteristic of a complex skewed flow. Not until further downstream of the belt trailing edge for $x'/\delta \geqslant 0.5$ does the hodograph exhibit the expected triangular shape with the apex of the triangle decreasing with streamwise distance. The belt width is too narrow (in the streamwise direction) for the flow to reach the collateral condition.

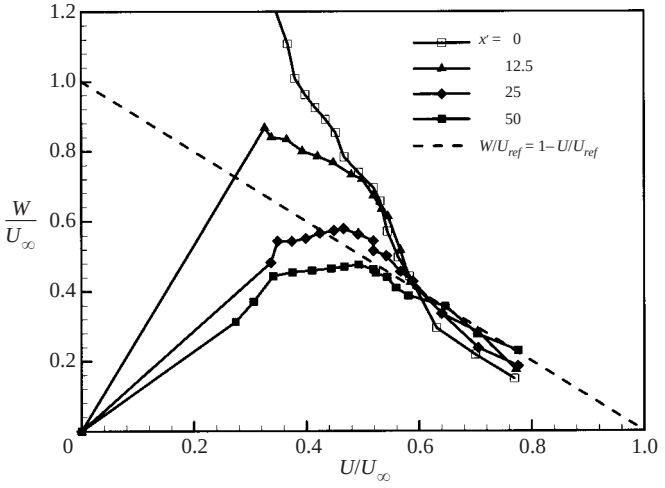

FIGURE 20. Hodograph plot for velocity ratio of $W_r = 2.75$.

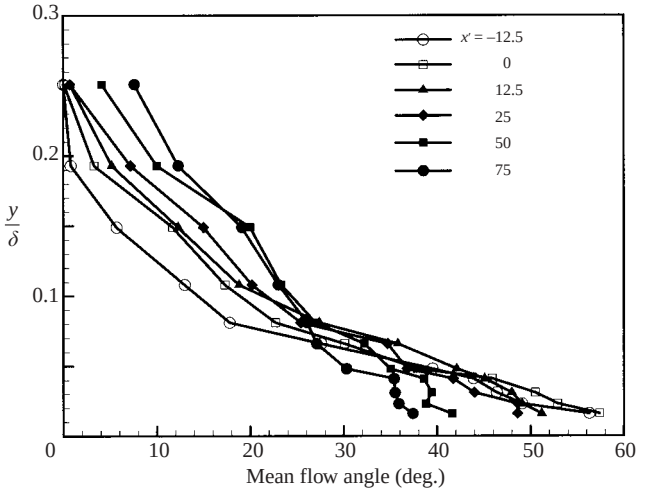

FIGURE 21. Mean flow angles for velocity ratio of $W_r = 2.75$.

Mean flow turning angles (defined as *ccw* with respect to the streamwise coordinate axis, x) are plotted in figure 21 for six streamwise locations over the belt surface and downstream of the belt trailing edge for the most strongly sheared case of $W_r = 2.75$. At the trailing edge of the belt, $x'/\delta = 0$, the maximum flow angle is 59° near the wall and quickly decays to zero by $y/\delta \approx 0.22$. The maximum mean flow angle decreases to approximately 40° near the wall surface at the downstream locations of $x'/\delta = 1.0$ and 1.5 and diminishes to approximately 5° by $y/\delta \approx 0.22$. In general, the effects of the spanwise shear on the mean flow field appear to be limited to the inner region of the boundary layer and confined to $y/\delta < 0.25$.

Profiles of the normal Reynolds stress, $\overline{u'^2}$, are plotted in figure 22 for $W_r = 0$, 1.0, 2.0 and 2.75 at the aforementioned four streamwise locations. The profiles are obtained from the average of three columns of PIV velocity vectors to reduce the

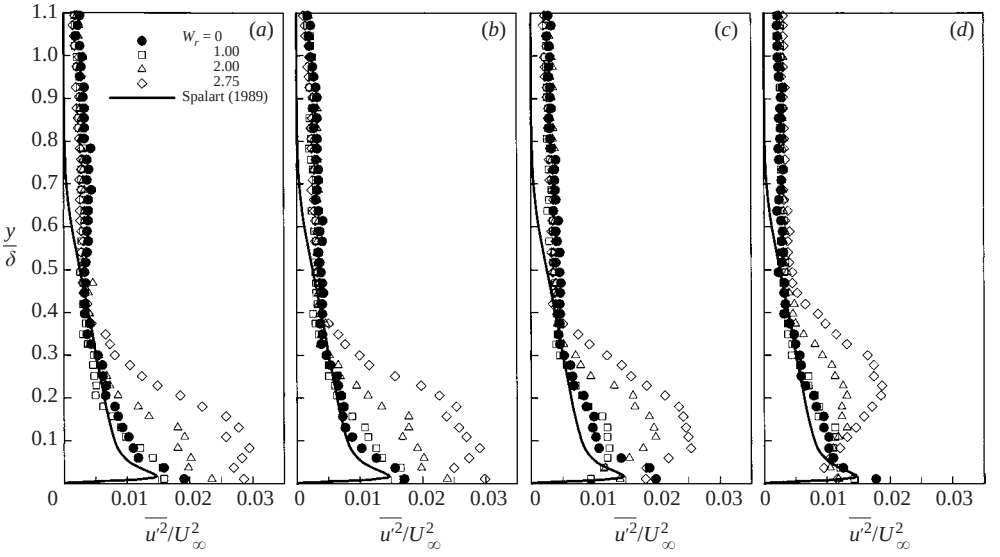

FIGURE 22. Profiles of $\overline{u'^2}$ normal Reynolds stress at (*a*) $x'/\delta = -0.25$, (*b*) $x'/\delta = 0$, (*c*) $x'/\delta = 0.25$, and (*d*) $x'/\delta = 1.0$ for velocity ratios of $W_r = 0$, 1.0, 2.0 and 2.75.

statistical scatter, i.e. spatially averaged over 1.7 mm, or 0.04δ (750 points used in the average). Over the belt surface ($x'/\delta = -0.25$), the crossflow causes a significant increase in the $\overline{u'^2}$ stress in the inner region of the boundary layer. In general, $\overline{u'^2}$ in the mildly sheared case of $W_r = 1.0$ is very similar to the two-dimensional base case. It is only for the more highly sheared cases of $W_r = 2.0$ and 2.75 that the effects of the crossflow become apparent. For the most highly sheared case of $W_r = 2.75$, the $\overline{u'^2}$ stress reaches a magnitude of approximately 0.03 U_∞^2 and the peak value occurs around $y/\delta \approx 0.1$. The effects of the crossflow extend into the boundary layer out to $y/\delta \approx 0.4$, beyond which the profiles collapse onto a common curve in the outer region of the boundary layer. The magnitude of the $\overline{u'^2}$ stress decreases with streamwise distance and the peak value in $\overline{u'^2}$ monotonically shifts further out into the boundary layer, with the effects of the crossflow extending out to $y/\delta \approx 0.6$. Another noteworthy feature of the two highly sheared cases ($W_r = 2.0$ and 2.75) is that there is an initial decrease in the $\overline{u'^2}$ normal stress in the near-wall region ($y/\delta < 0.05$) which quickly recovers and reaches increased values compared to the $W_r = 0$ and 1.0 cases.

Corresponding profiles for the $\overline{v'^2}$ normal Reynolds stress are plotted in figure 23. Spanwise shear causes a monotonic increase in the $\overline{v'^2}$ normal stress away from the wall. Similar to the $\overline{u'^2}$ stress profiles, there is a significant increase in the $\overline{v'^2}$ stress over the belt surface at $x'/\delta = -0.25$ with increasing spanwise shear. For the most highly sheared case of $W_r = 2.75$, the peak value is approximately 0.14 U_∞^2 and occurs at $y/\delta \approx 0.1$. This peak in $\overline{v'^2}$ shifts further out into the boundary layer with increased spanwise shear, and the effects of the crossflow extend out to $y/\delta \approx 0.3$. At the downstream position ($x'/\delta = 2.0$) the magnitude of the $\overline{v'^2}$ stress is still quite large compared to the two-dimensional base case. The peak in the $\overline{v'^2}$ stress levels continues to shift further out into the boundary layer with increasing spanwise shear.

Profiles of the primary Reynolds shear stress, $-\overline{u'v'}$, are presented in figure 24. As the normal stresses, these profiles use the spatial average of three columns of

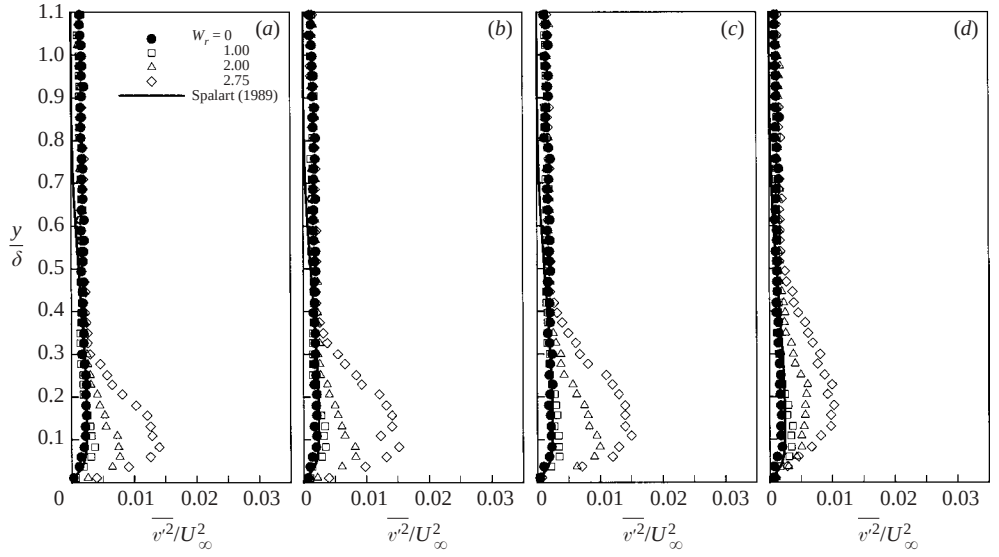

FIGURE 23. Profiles of $\overline{v'^2}$ normal Reynolds stress at (*a*) $x'/\delta = -0.25$, (*b*) $x'/\delta = 0$, (*c*) $x'/\delta = 0.25$, and (*d*) $x'/\delta = 1.0$ for velocity ratios of $W_r = 0$, 1.0, 2.0 and 2.75.

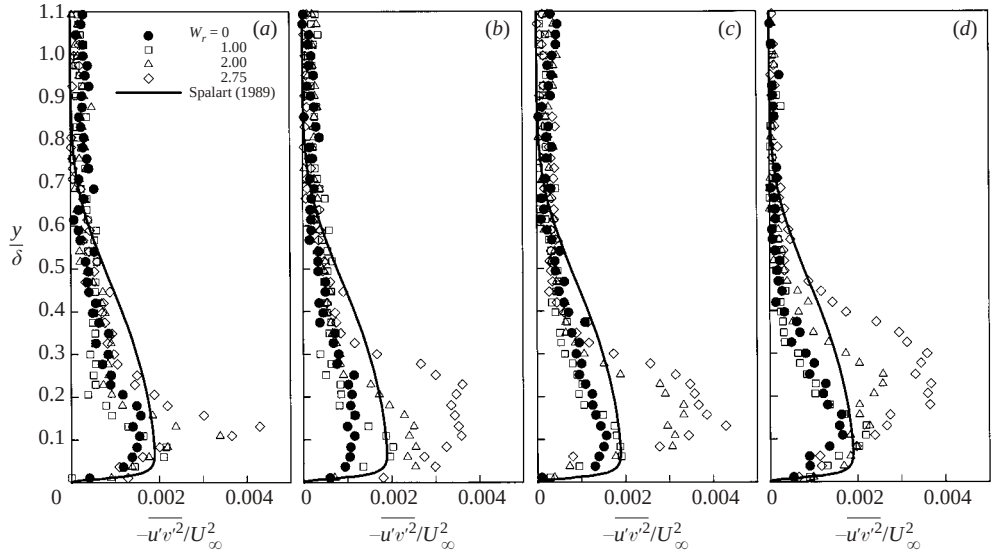

FIGURE 24. Profiles of $-\overline{u'v'}$ Reynolds shear stress at (*a*) $x'/\delta = -0.25$, (*b*) $x'/\delta = 0$, (*c*) $x'/\delta = 0.25$, and (*d*) $x'/\delta = 1.0$ for velocity ratios of $W_r = 0$, 1.0, 2.0 and 2.75.

PIV velocity vectors to reduce the scatter. Over the belt surface at $x'/\delta = -0.25$, the spanwise shear results in a sharp increase in the magnitude of $-\overline{u'v'}$, particularly for the most highly sheared cases of $W_r = 2.0$ and 2.75. The peak in the $-\overline{u'v'}$ shear stress at the first measuring station for all four velocity ratios occurs at approximately $y/\delta \approx 0.1$ and the increase in the shear stress over the base case is limited to $y/\delta < 0.3$ for the $W_r = 2.75$ case. At the subsequent measuring station, the trailing edge of the belt ($x' = 0$), the effects of the crossflow on $-\overline{u'v'}$ are clearer. The mildly sheared

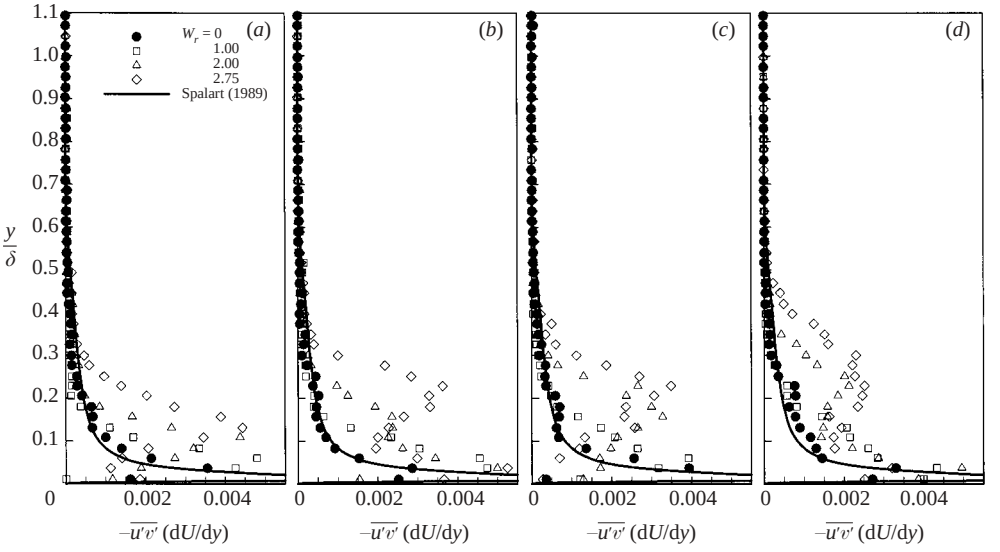

FIGURE 25. Profiles of turbulence production, $-\overline{u'v'}(\partial U/\partial y)$, at (*a*) $x'/\delta = -0.25$, (*b*) $x'/\delta = 0$, (*c*) $x'/\delta = 0.25$, and (*d*) $x'/\delta = 1.0$ for velocity ratios of $W_r = 0$, 1.0, 2.0 and 2.75.

case of $W_r = 1.0$ exhibits a mild increase in $-\overline{u'v'}$ over the two-dimensional case, for $y/\delta < 0.1$. The more highly sheared cases of $W_r = 2.0$ and 2.75 exhibit a larger increase in the magnitude of $-\overline{u'v'}$. The $W_r = 2.0$ case exhibits a 100% increase, while the $W_r = 2.75$ case exhibits a 140% increase in $-\overline{u'v'}$. Another effect of the crossflow is to shift the peak in the $-\overline{u'v'}$ shear stress away from the wall with increased spanwise strain. For the two-dimensional base case, the peak in $-\overline{u'v'}$ is located at $y/\delta \approx 0.1$, while for the most highly sheared case of W_r=2.75 the peak has shifted out to $y/\delta \approx 0.2$. Although three-dimensionality generally results in a reduction of the Reynolds shear stresses and the a_1 parameter, the regions where the boundary layer is initially skewed exhibit an overshoot of $-\overline{u'v'}$. This trend has been reported in other studies (e.g. Flack & Johnston 1994; Compton & Eaton 1997). At subsequent downstream locations the effects of the crossflow on the primary Reynolds stress diffuse out into the boundary layer. This is indicated by a continuous shift in the peak of the $-\overline{u'v'}$ shear stress further into the outer region of the boundary layer, as well as increased levels of $-\overline{u'v'}$ extending out to $y/\delta \approx 0.6$ at the downstream profile locations. However, the magnitude of the $-\overline{u'v'}$ stress begins to decrease slightly, showing signs of a relaxing flow field.

Plots of the primary turbulent shear stress production, $-\overline{u'v'}(\partial U/\partial y)$, are presented in figure 25 for belt velocity ratios of $W_r = 0$, 1.0, 2.0 and 2.75 at five streamwise profile measurement stations. The effect of the increasing crossflow is to increase the magnitude of $-\overline{u'v'}(\partial U/\partial y)$ over the belt surface at $x'/\delta = -0.25$ and at the belt trailing edge ($x'/\delta = 0$), with peak values of the order of $0.0045\,\mathrm{m^2\,s^{-3}}$ near the belt surface. At subsequent measuring stations, the magnitude of production for the more highly sheared cases of $W_r = 2.0$ and 2.75 decreases compared to the upstream stations, but is still elevated above the two-dimensional base case. Although the magnitude decreases (to approximately $0.002\,\mathrm{m^2\,s^{-3}}$), the associated peak value shifts further away from the wall out to $y/\delta \approx 0.25$ at $x'/\delta = 0.5$. The magnitude of primary

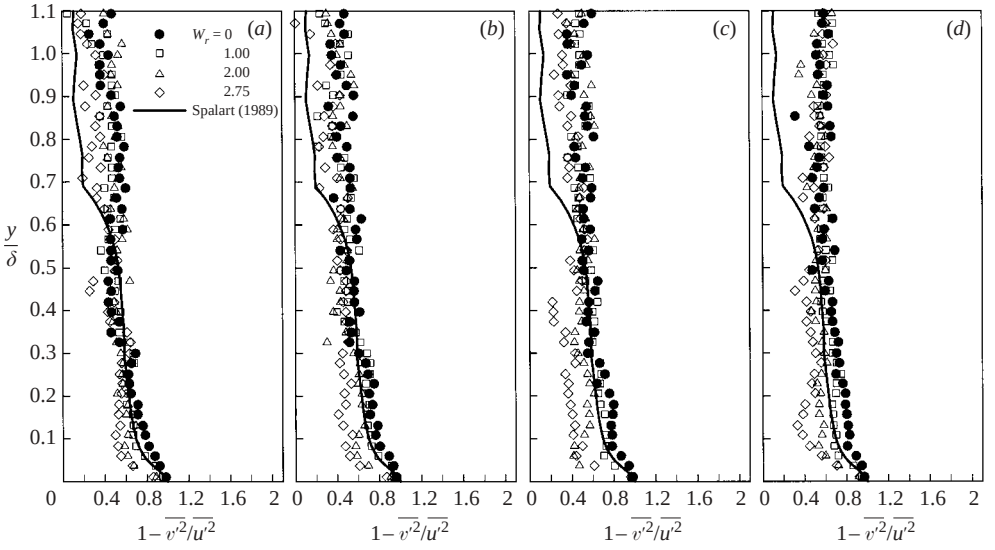

FIGURE 26. Profiles of $1 - v'^2/u'^2$ anisotropy at (*a*) $x'/\delta = -0.25$, (*b*) $x'/\delta = 0$, (*c*) $x'/\delta = 0.25$, and (*d*) $x'/\delta = 1.0$ for velocity ratios of $W_r = 0$, 1.0, 2.0 and 2.75.

shear stress production continues to decrease with streamwise distance as the $-\overline{u'v'}$ shear stress diffuses into the boundary layer and the transverse velocity gradient, $\partial U/\partial y$, is reduced. Although the magnitude of $-\overline{u'v'}(\partial U/\partial y)$ at the downstream measuring stations is lower than at the upstream locations over the belt surface, production levels extend further into the boundary layer out to $y/\delta \approx 0.5$ where they eventually return to two-dimensional levels.

Profiles of $(1 - \overline{v'}^2/\overline{u'}^2)$ are presented in figure 26. The magnitude of this quantity, which is an approximate anisotropy (strictly defined by the tensor *bij*), is significantly reduced for the more highly sheared cases of $W_r = 2.0$ and 2.75 over the belt surface at $x'/\delta = -0.25$. In the inner region of the boundary layer the levels of $(1 - \overline{v'}^2/\overline{u'}^2)$ are almost half those of the two-dimensional case ($W_r = 0$). Downstream of the belt trailing edge, at $x'/\delta = 0.25$, the magnitude of $(1 - \overline{v'}^2/\overline{u'}^2)$ remains suppressed compared to two-dimensional values in the inner region of the boundary layer and elevated levels are only observed in the near-wall region. At the downstream measuring stations, the magnitude of $(1 - \overline{v'}^2/\overline{u'}^2)$ for the two highly imposed spanwise shear cases of $W_r = 2.0$ and 2.75 remains consistently lower than that of the $W_r = 0$ case at wall-normal distances below $y/\delta \approx 0.3$. In the outer region of the boundary layer ($y/\delta > 0.4$) the magnitude of $(1 - \overline{v'}^2/\overline{u'}^2)$ in the flow field is essentially the same for all four cases and is reduced compared to values in the inner region of the boundary layer. The slow recovery of this quantity to two-dimensional levels at the downstream measuring locations is a result of a more rapid reduction of the u'^2 normal stress from its peak value over the belt surface compared to the somewhat slower diffusion of the v'^2 normal stress in the inner region of the boundary layer. Profiles of a similar 'anisotropy' in the spanwise direction, $(1 - \overline{w'}^2/\overline{u'}^2)$ for velocity ratio $W_r = 2.75$ were also examined. However, the magnitude of this quantity could not be determined accurately from the available data and therefore the full extent of the anisotropy of this shear-driven 3DTBL is not known.

Eddy-viscosity models are most typically applicable to 2DTBLs, with monotonically increasing velocities in the boundary layer. Flow fields, which exhibit profiles with local maxima or minima, represent more challenging cases for the application of an eddy-viscosity model and the skewed velocity profile in a 3DTBL is certainly one of these. For computational simplicity, the eddy viscosity is often replaced by a mixing-length term. The mixing length, l_{mix}, represents a characteristic mean eddy size in the flow field and is given by

$$-\overline{u'v'} = l_{mix}^2 \left(\frac{\partial U}{\partial y}\right)^2. \tag{1}$$

This definition of the mixing length, however, is most applicable for two-dimensional flows and a more accurate definition for a 3DTBL should take into account secondary Reynolds stresses, as well as other rates of strain. Bradshaw (1987) discusses a revised definition for three-dimensional flows that is given by

$$\sqrt{\overline{u'v'}^2 + \overline{v'w'}^2} = l_{mix}^2 \left[\left(\frac{\partial U}{\partial y}\right)^2 + \left(\frac{\partial W}{\partial y}\right)^2\right]. \tag{2}$$

Because of the lack of $\overline{v'w'}$ data in this experiment and the limited amount of information on $\partial W/\partial y$, the two-dimensional definition of the mixing length (equation (1)) was applied, recognizing the limitations of this approach.

In the case of wall-bounded shear flow, the mixing length is proportional to the distance from the surface. In the inner region of the boundary layer the mixing length can be expressed by a single equation developed by van Driest (White 1991) and given by

$$l_{mix} = \kappa y \left[1 - \exp\left(-\frac{y^+}{A}\right)\right], \tag{3}$$

where $A = 26$ for flat-plate flows. In the outer region of the boundary layer, the mixing length can be expressed as a function of the boundary layer thickness and is typically given by

$$l_{mix} = 0.09\delta. \tag{4}$$

Profiles of the mixing length are shown in figure 27 for the four belt velocity ratios of $W_r = 0$, 1.0, 2.0 and 2.75. A piecewise curve fit (a fifth-order polynomial in the inner region and a second-order polynomial in the outer region) was applied to the mean velocity profile in order to provide a smoother estimate of the velocity gradient, $\partial U/\partial y$, used in calculating l_{mix}. This was done in order to reduce the scatter in the mixing-length calculation, where a relatively small $-\overline{u'v'}$ value is divided by an even smaller velocity gradient term in the outer region of the boundary layer. Consequently, the scatter in the mixing-length results increases significantly beyond $y/\delta = 0.5$ and, therefore, the profiles are limited to $y/\delta < 0.7$ to highlight the inner region of the boundary layer. The mixing-length profiles are normalized by the boundary-layer thickness and compared to the two-dimensional expressions described above (the van Driest approximation in the inner region and $l_{mix} = 0.09\delta$ in the outer region). In the region near the wall, below $y/\delta < 0.1$, the mixing length agrees with the van Driest approximation reasonably well, i.e. the more highly sheared cases ($W_r = 2.0$ and 2.75) do not deviate significantly from the two-dimensional base case ($W_r = 0$). In general, the mixing-length profiles for the more highly sheared cases tend to deviate from the van Driest approximation and appear to asymptote to values of l_{mix}/δ lower than 0.09 in the boundary layer beyond $y/\delta > 0.4$. For the most highly sheared cases of $W_r = 2.0$ and 2.75 the l_{mix}/δ value approaches 0.05.

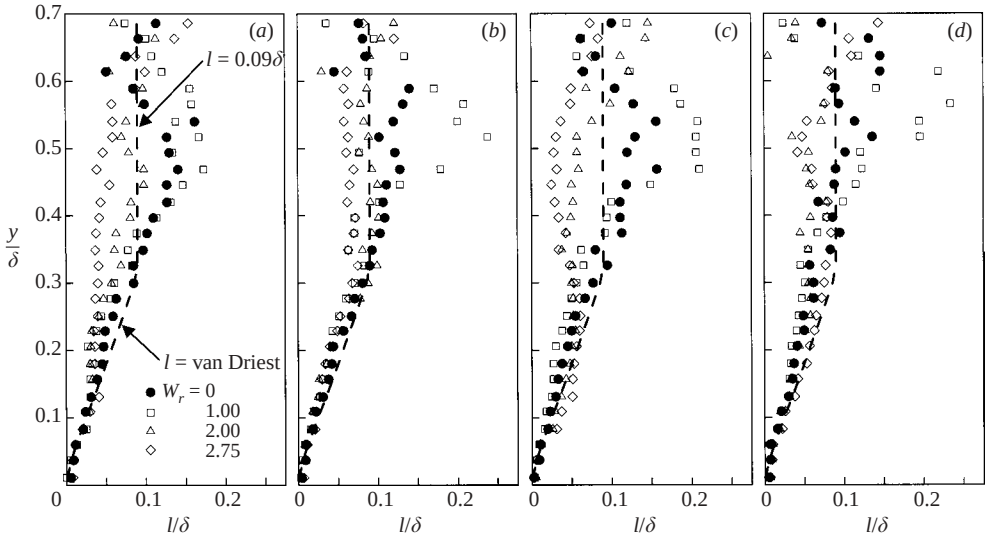

FIGURE 27. Profiles of mixing length, l, at (a) $x'/\delta = -0.25$, (b) $x'/\delta = 0$, (c) $x'/\delta = 0.25$, and (d) $x'/\delta = 1.0$ for velocity ratios of $W_r = 0$, 1.0, 2.0 and 2.75.

These trends are consistent with observations made by Littell & Eaton (1994) in their rotating disk flow, although in their case, the deviation was more pronounced. This is most probably due to their use of the three-dimensional definition of l_{mix} given in (2). The profiles of the l_{mix} presented in figure 27 suggest that the use of a two-dimensional mixing-length model could perhaps be effective in the innermost region of the shear-driven 3DTBL. However, for the most highly sheared cases, the $l_{mix} = 0.09\delta$ approximation in the outer region of the boundary layer generally overpredicts the mixing-length data, although the large scatter precludes making definitive conclusions.

5. Conclusions

A planar shear-driven three-dimensional turbulent boundary layer was generated using a shear-generating mechanism that provided varying degrees of crossflow. Investigation of the resulting non-equilibrium three-dimensional turbulent boundary layer revealed significant modifications of the near-wall flow physics. LIF flow visualization indicated that the near-wall low-speed streak structure is affected by crossflow.

PIV measurements further quantified modifications of the inner region of the turbulent boundary layer due to crossflow. Velocity field measurements in both the (x, y)-plane (perpendicular to the wall) and (x, z)-plane (plan view) exhibited significant disruption of flow structures at higher imposed shear compared to a 2DTBL. Fluctuating velocity fields exhibited an increase in magnitude and stronger vortical regions with circular streamlines throughout the inner region of the boundary layer with increasing spanwise shear. An additional effect of the crossflow was the disruption of both spanwise and transverse vorticity layers in the near-wall region compared to that in the two-dimensional base case. The interaction of flow structures and increased levels and distortion of both spanwise and transverse vorticity reorient

near-wall vortical structures (e.g. legs of hairpins), which are associated with elongated streak structures. The disruption of near-wall vorticity (by the structures) results in the breakup of the near-wall streaks and lifts them into the inner region of the boundary layer at an advanced stage compared to the two-dimensional case.

The major findings of this experimental investigation of a planar shear-driven 3DTBL with varying degrees of crossflow can be summarized as follows:

Visualization of the near-wall streak structure indicates that the crossflow disrupts the streak structure, resulting in a 50% reduction in mean streamwise streak length and no significant modification of streak spacing. The reduction of streamwise length scales is confirmed by streamwise velocity spectra. The distortion of the near-wall streak structure observed in this study is consistent with numerical studies by Sendstad & Moin (1992), Le *et al.* (1999) and Kannepalli & Piomelli (2000).

Spanwise shear results in numerous flow structures in the inner region of the boundary layer that are associated with enhanced momentum transfer and a thickening of the inner region of the turbulent boundary layer.

The two-dimensional spanwise vorticity layer on the wall surface is severely disrupted with increased crossflow, resulting in vortices of opposite sign lifting off the wall surface and diffusing into the boundary layer with streamwise distance. The transverse vorticity experiences a similar transformation with increased spanwise shear, particularly over the translating wall section. These multiple vortex interactions disrupt the alignment of vortical structures in the near-wall region affecting turbulence generation.

Mean flow data indicate a significant deficit in the streamwise velocity with increased crossflow in the region $y/\delta < 0.4$. Spanwise velocity rapidly diminishes with wall-normal distance indicating that three-dimensional effects are confined to a narrow region along the wall surface ($y/\delta < 0.2$), and convect outward with streamwise distance.

The normal Reynolds stresses, $\overline{u'^2}$, $\overline{v'^2}$ and $\overline{w'^2}$ increase in the inner region of the boundary layer with increasing spanwise shear, particularly over the translating wall section.

The magnitude of the Reynolds shear stresses, $-\overline{u'v'}$ and $-\overline{u'w'}$, increases in the inner region of the boundary layer and the peak values shift away from the wall with increased crossflow.

The spanwise shear results in a significant increase of the turbulent kinetic energy in the near-wall region compared to the two-dimensional base case. The increase in TKE is particularly large over the translating wall section and gradually decreases with streamwise distance.

Turbulent eddy viscosity and corresponding mixing-length approximations indicate that, in the innermost region of this shear-driven 3DTBL, the van Driest model for l_{mix} may be suitable for predicting the primary Reynolds shear stress.

The imposed spanwise shear leads to increased turbulence generation concentrated near the wall ($y/\delta < 0.2$) over the belt surface. An internal boundary layer forms over the moving belt surface and another at the trailing edge of the belt where there is a discontinuity in the wall velocity boundary condition. It is proposed that the crossflow induces skewing and stretching of the tail region of hairpin vortices in the direction of the spanwise shear. The resulting generation of flow structures in the inner region of the boundary layer transports the energy introduced by the translating belt throughout the boundary layer. This transport mechanism enhances Reynolds shear

stresses. Increased turbulence production over the translating wall section results in an increase in turbulent kinetic energy and the Reynolds shear stresses, $-\overline{u'v'}$ and $-\overline{u'w'}$. It is recommended that more complete measurements are made of all of the components of the Reynolds shear stress to further elucidate the flow.

REFERENCES

Adrian, R., Meinhart, C. & Tomkins, C. 2000 Vortex organization in the outer region of the turbulent boundary layer. *J. Fluid Mech.* **422**, 1–54.

Anderson, S. & Eaton, J. 1987 Experimental study of a pressure-driven, three-dimensional, turbulent boundary layer. *AIAA J.* **25**, 1086–1092.

Anderson, S. & Eaton, J. 1989 Reynolds stress development in pressure-driven three-dimensional turbulent boundary layers. *J. Fluid Mech.* **202**, 263–294.

Bissonnette, L. & Mellor, G. 1974 Experiments on the behaviour of an axisymmetric turbulent boundary layer with a sudden circumferential strain. *J. Fluid Mech.* **63**, 369–413.

Bradshaw, P. 1987 Turbulent secondary flows. *Annu. Rev. Fluid Mech.* **19**, 53–73.

Bradshaw, P. & Pontikos, N. S. 1985 Measurements in the turbulent boundary layer on an 'infinite' swept wing. *J. Fluid Mech.* **159**, 105–130.

Cater, J. & Soria, J. 2001 PIV measurements of turbulent jets. *4th Intl Symp. Particle Image Velocimetry, Göttingen, Germany*, P1019.

Chiang, C. & Eaton, J. 1996 An experimental study of the effects of three-dimensionality on the near wall turbulence structures using flow visualization. *Exps. Fluids* **20**, 266–272.

Coleman, G., Kim, J. & Le, A. 1996 A numerical study of three-dimensional wall-bounded flows. *Intl J. Heat Fluid Flow* **17**, 333–342.

Coleman, G., Kim, J. & Spalart, P. 2000 A numerical study strained three-dimensional wall-bounded turbulence. *J. Fluid Mech.* **416**, 75–116.

Compton, D. & Eaton, J. 1997 Near-wall measurements in a three-dimensional turbulent boundary layer. *J. Fluid Mech.* **350**, 189–208.

Driver, D. & Hebbar, S. 1987 Experimental study of a three-dimensional, shear-driven, turbulent boundary layer. *AIAA J.* **25**, 35–42.

Driver, D. & Hebbar, S. 1989 Three-dimensional shear-driven boundary-layer flow with streamwise adverse pressure gradient. *AIAA J.* **27**, 1689–1697.

Driver, D. & Johnston, J. 1990 Experimental study of a three-dimensional shear-driven turbulent boundary layer with streamwise adverse pressure gradient. *NASA TM* 102211.

Eaton, J. 1995 Effects of mean flow three dimensionality on turbulent boundary-layer structure. *AIAA J.* **33**, 2020–2025.

Flack, K. & Johnston, J. 1993 Near-wall investigation of three-dimensional turbulent boundary layers. *Rep. MD* 63. Thermosci. Div. Mech. Engng, Stanford University.

Flack, K. & Johnston, J. 1994 Near-wall flow in a three-dimensional turbulent boundary layer on the endwall of a rectangular bend. *AIAA Paper* 94-0405.

Johnston, J. & Flack, K. 1996 Advances in three-dimensional turbulent boundary layers with emphasis on the wall-layer regions. *Trans. ASME* I: *J. Fluids Engng* **118**, 219–232.

Kannepalli, C. & Piomelli, U. 1999 Large-eddy simulation of a three-dimensional shear-driven turbulent boundary layer. *3rd ERCOFTAC Workshop on Direct and Large-Eddy Simulation*, Cambridge, *UK*.

Kannepalli, C. & PioMelli, U. 2000 Large-eddy simulation of a three-dimensional shear-driven turbulent boundary layer. *J. Fluid Mech.* **423**, 175–203.

Kiesow, R. 1994 Design and Qualification of a Recirculating water tunnel for 3-D boundary layer studies. MS thesis, School of Mechanical Engineering, Purdue University.

Kiesow, R. 2000 Investigation of a shear-driven 3-D turbulent boundary layer with varying crossflow. PhD thesis, School of Mechanical Engineering, Purdue University.

Kiesow, R. & Plesniak, M. 1997 Near-wall physics and structure of a shear-driven 3-D turbulent boundary layer. *ASME FED Symp. on Complex and Separated Flows, Vancouver BC*, FEDSM97-3282.

Kiesow, R. & Plesniak, M. 1998 Modification of near-wall turbulence structure in a shear-driven three-dimensional turbulent boundary layer. *Exps. Fluids* **25**, 233–242.

KIESOW, R. & PLESNIAK, M. 1999*a* Structural modifications and near-wall physics of a shear-driven 3-D turbulent boundary layer. *ASME FED Symp. on Separated and Complex Flows, San Francisco, CA*, FEDSM99-7068.

KIESOW, R. & PLESNIAK, M. 1999*b* Modification of near-wall structure in a three-dimensional turbulent boundary layer. In *Turbulence and Shear Flow Phenomena 1999–1* (ed. S. Banerjee & J. Eaton), pp. 157–162. Begell House, NY.

KIESOW, R. & PLESNIAK, M. 2001 Turbulence modifications in a planar shear-driven 3-d turbulent boundary layer. *ASME FED Symp. on Separated & Complex Flows, New Orleans, LA*. FEDSM01-18105.

KIESOW, R. & PLESNIAK, M. 2002 Modification of near-wall structure in a shear-driven 3-D turbulent boundary layer. *Trans. ASME* I: *J. Fluids Engng* **124**, 118–126.

LE, A. 1999 A numerical study of three-dimensional turbulent boundary layers. PhD thesis, University of California.

LE, A., COLEMAN, G. & KIM, J. 1999 Near-wall turbulence structures in three-dimensional boundary layers. *Proc. First Intl Symp. on Turbulence and Shear Flow Phenomena*, pp. 147–152.

LITTELL, H. & EATON, J. 1994 Turbulence characteristics of the boundary layer on a rotating disk. *J. Fluid Mech.* **266**, 175–207.

LOHMANN, R. 1976 The response of a developed turbulent boundary layer to local transverse surface motion. *Trans. ASME* I: *J. Fluids Engng* **98**, 354–363.

MOFFAT, R. 1988 Describing the uncertainties in experimental results. *Expl Thermal Fluid Sci.* **1**, 3–17.

MOIN, P., SHIH, T., DRIVER, D. & MANSOUR, N. 1990 Direct numerical simulation of a three-dimensional turbulent boundary layer. *Phys. Fluids* **2**, 1846–1853.

ÖLÇMEN, M. & SIMPSON, R. 1992 Perspective: On the near wall similarity of three-dimensional turbulent boundary layers. *Trans. ASME*: *J. Fluids Engng* **114**, 487–495.

ÖLÇMEN, M. & SIMPSON, R. 1995 An experimental study of a three-dimensional pressure-driven turbulent boundary layer. *J. Fluid Mech.* **290**, 225–262.

ROBINSON, S. 1991 Motions in the turbulent boundary layer. *Annu. Rev. Fluid Mech.* **23**, 601–639.

SCHWARZ, W. & BRADSHAW, P. 1993 Measurements in a pressure-driven three-dimensional turbulent boundary layer during development and decay. *AIAA J.* **7**, 1207–1214.

SCHWARZ, W. & BRADSHAW, P. 1994 Turbulence structural changes for a three-dimensional turbulent boundary layer in a 30° bend. *J. Fluid Mech.* **272**, 183–209.

SENDSTAD, O. & MOIN, P. 1992 The near-wall mechanics of three-dimensional turbulent boundary layers. *Rep. TF* 57. Thermosci. Div. Mech. Engng, Stanford University.

SPALART, P. 1989 Theoretical and numerical study of a three-dimensional turbulent boundary layer. *J. Fluid Mech.* **205**, 319–340.

UZOL, O. & CAMCI, C. 2001 The effect of sample size, turbulence intensity and the velocity field on the experimental accuracy of ensemble averaged PIV measurements. *4th Intl Symp. on Particle Image Velocimetry, Götingen, Germany*, P1096.

WEBSTER, D., DEGRAAFF, D. & EATON, J. 1996 Turbulence characteristics of a boundary layer over a swept bump. *J. Fluid Mech.* **323**, 1–22.

WHITE, F. 1991 *Viscous Fluid Flow*, 2nd Edn. McGraw-Hill.

WU, X. & SOUIRES, K. 1997 Large eddy simulation of an equilibrium three-dimensional turbulent boundary layer. *AIAA J.* **35**, 67–74.

WU, X. & SOUIRES, K. 1998 Prediction of the three-dimensional turbulent boundary layer over a swept bump. *AIAA J.* **36**, 505–514.

ZHOU, J., ADRIAN, R., BALACHANDAR, S. & KENDALL, T. 1999 Mechanism for generating coherent packets of hairpin vortices in channel flow. *J. Fluid Mech.* **387**, 353–396.